



Ultrafast degradation of emerging organic pollutants via activation of peroxymonosulfate over $\text{Fe}_3\text{C}/\text{Fe@N-C-x}$: Singlet oxygen evolution and electron-transfer mechanisms

Chen Zhao^a, Linghui Meng^a, Hongyu Chu^a, Jian-Feng Wang^b, Tianyu Wang^a, Yuhui Ma^c, Chong-Chen Wang^{a,*}

^a Beijing Key Laboratory of Functional Materials for Building Structure and Environment Remediation, Beijing University of Civil Engineering and Architecture, Beijing 100044, China

^b Institute of Analysis and Testing, Beijing Academy of Science and Technology (Beijing Center for Physical & Chemical Analysis), Beijing Engineering Research Center of Food Safety Analysis, Beijing 100089, China

^c Key Laboratory for Biomedical Effects of Nanomaterials and Nanosafety, Institute of High Energy Physics, Chinese Academy of Sciences, Beijing 100049, China

ARTICLE INFO

Keywords:

MIL-88B(Fe)
Melamine
Peroxymonosulfate
Singlet oxygen
Electron-transfer

ABSTRACT

$\text{Fe}_3\text{C}/\text{Fe}$ decorated N-doped magnetic carbon materials (denoted as $\text{Fe}_3\text{C}/\text{Fe@N-C-x}$) were successfully fabricated via facile one-pot calcination of MIL-88B(Fe) with a green precursor of melamine. Benefiting from the co-existence of sp^2 -hybridized C- π moieties, oxygen-containing groups (C=O and O-C=O), N-doping species and ferrous nanoparticles (FNPs), the as-obtained $\text{Fe}_3\text{C}/\text{Fe@N-C-9}$ exhibited excellent activation of peroxymonosulfate (PMS) for ultrafast elimination of various emerging organic contaminants with high mineralization capacities. Inspired by the unique nanotube morphology and encapsulation of FNPs, the $\text{Fe}_3\text{C}/\text{Fe@N-C-9}$ possessed trace Fe leaching and can be magnetically separated for an easy recycling. Combining with competitive radical scavenging tests, electron spin resonance (ESR), electrochemical analysis and *in-situ* Raman spectra, the singlet oxygen ($^1\text{O}_2$) and electron-transfer can be accounted for the organic pollutant removal. Because of that, the $\text{Fe}_3\text{C}/\text{Fe@N-C-9}$ exhibited good resistance to inorganic anions and natural organic matters (NOMs). It was fascinating that $\text{Fe}_3\text{C}/\text{Fe@N-C-9}$ achieved satisfactory treatment efficiency for real pharmaceutical wastewater.

1. Introduction

Recently, with the progress of technology and rapid development of industrialization, new chemicals have been produced in large quantities to meet the needs of multiple application fields. Nevertheless, as everything has two sides, a few organic pollutants such as pharmaceutical and personal care products, microplastics, endocrine disrupting chemicals, per- and polyfluorinated chemicals have been frequently detected in different water environments owing to their non-biodegradability, persistence and ecotoxicity properties, giving rise to potential risks to life health and eco-environment [1,2]. Advanced oxidation processes (AOPs), in which the *in-situ* generated oxygen species (ROSs) with strong oxidation capacities are capable of decomposing and mineralizing organic compounds into harmless products in aqueous media, have gained increasing attention for the elimination of refractory organic pollutants in wastewater [3,4]. Among them, persulfate-based

AOPs (PS-AOPs) have been certified as progressive technologies to produce a few varieties of ROSs, such as sulfate ($\text{SO}_4^{\cdot-}$), hydroxyl ($\cdot\text{OH}$) and peroxide ($\cdot\text{O}_2$) radicals [5–7]. But for real wastewater treatments, the co-existence of natural organic matters (NOMs) and inorganic anions might significantly influence the catalytic performance of a radical-based AOP system via scavenging the highly oxidizing ROSs. Meanwhile, the weakened oxidation capacity leads to incomplete mineralization of organic pollutants and production of toxic secondary intermediates, ultimately limiting its potential applications in complex wastewater matrices [8].

By contrast, heterogeneous catalytic activated persulfate reaction systems based on non-radical pathways have attracted much attention due to its inapproachable advantages. Three mainstream non-radical pathways have been diffusely studied, including singlet oxygen ($^1\text{O}_2$) evolution, electron-transfer process and high-valent metal induced oxidation [9]. In general, the oxidizabilities of the non-radical systems

* Corresponding author.

E-mail addresses: wangchongchen@bucea.edu.cn, chongchenwang@126.com (C.-C. Wang).

<https://doi.org/10.1016/j.apcatb.2022.122034>

Received 29 June 2022; Received in revised form 22 September 2022; Accepted 29 September 2022

Available online 10 October 2022

0926-3373/© 2022 Elsevier B.V. All rights reserved.

are moderate compared with the strongly oxidizing ROSs-based systems. Nevertheless, non-radical oxidation processes several outstanding superiorities over oxidation reactions relied on reactive radicals in real wastewater treatment. Such as (1) electron-rich organic pollutants are inclined to be catalytic degradation with high selectivity [10]; (2) the catalytic efficiencies of non-radical oxidation systems can still be appreciable over a broad pH range and in complex wastewater matrices, despite the co-existence of inorganic anions and NOMs [8,11]; (3) Being compared with traditional AOPs, peroxides can be efficiently utilized with low stoichiometry between the consumed persulfate and target organic pollutants during non-radical processes, which is beneficial to prominently reduce chemical inputs and is more economical for wastewater treatment [10,12] and (4) the reaction pathways and redox potentials of non-radical systems can be further optimized via regulating the structure and composition of the catalysts. Therefore, developing an efficient and green catalytic system based on non-radical process is more meaningful and feasible for treatment of refractory organic wastewater.

Currently, carbon-based catalysts including reduced graphene oxide (rGO) [13], carbon nanotubes (CNTs) [10], nanodiamonds [14] and biochar [15] have been employed as heterogeneous catalysts for mediating non-radical processes, especially $^1\text{O}_2$ evolution and electron-transfer mechanisms. The impressive catalytic performances of the above carbonaceous materials can be attributed to the abundant sp^2 -hybridized carbon components with multifunctional active centers, such as ketonic groups and edges [16,17]. Moreover, during the catalytic process, the peroxydisulfate (PDS) or PMS can be activated by the conjugated π structures originated from graphitic carbons to generate a metastable complex, which was prone to trigger the oxidation of target organic pollutants via electron extraction without producing ROSs [10]. It was depressing that although the carbon-based materials showed good ability for PDS/PMS activation, which even exceeded the traditional MnO_2 , Fe_3O_4 , CuO and Co_3O_4 catalysts, these carbon-based catalysts still exhibited limited catalytic activities.

At present, considerable attempts have been made to improve the catalytic performances of carbon-based catalysts by combination of metal nanoparticles (MNPs) and proper doping of heteroatoms including nitrogen, phosphorus, sulfur and the other non-metallic elements [17]. Benefitting by the strong conductivity of MNPs, the presence of MNPs might effectively regulate the electronic structures of the interacted carbonaceous materials via interfacial electron transfer, which has indelibly improved the catalytic efficiencies of hydrogen evolution reaction (HER) and oxygen reduction reaction (ORR) [18,19]. Besides, the encapsulation of MNPs beneath the carbon shell may not merely endow the carbon-based materials with magnetic performance, but also protect MNPs against corrosion and leaching. Additionally, the doping of heteroatoms can initiate new properties to enhance the reactivity, selectivity, hydrophilicity and increase more reactive sites [20,21].

In this work, $\text{Fe}_3\text{C}/\text{Fe}$ decorated N-doped CNTs ($\text{Fe}_3\text{C}/\text{Fe@N-C-x}$, where x represented the calcination temperature divided by 100) were successfully prepared by facile calcination of the mixture of melamine and MIL-88B(Fe), which was simply obtained by ball-milling process without any other additions. With regard to the used precursors, melamine acted as N and C sources. As one type of metal-organic frameworks (MOFs), MIL-88B(Fe) possessed large specific surface area (up to $222.8\text{ m}^2/\text{g}$) [22]. More importantly, the excessive aggregation of FNP during the MIL-88B(Fe) carbonization process can be effectively restrained on account of the support by organic ligands and the evenly distribution of $\text{Fe}_3\text{-}\mu_3\text{-oxo}$ clusters [23]. Therefore, the harvest of uniform Fe^0 or Fe_3C nanoparticles was possible. Furthermore, the catalytic performances of the as-prepared $\text{Fe}_3\text{C}/\text{Fe@N-C-x}$ were evaluated by activating PMS for decomposition of different types of organic pollutants. The synergistic effect of sp^2 -hybridized carbon, oxygen-containing groups, encapsulation of FNPs and N-doping species for the improvement of catalytic performance was systematically investigated by advanced characterizations and selectively scavenging radical tests. The effects of various environmental factors on organic pollutants removal

as well as the reusability of the $\text{Fe}_3\text{C}/\text{Fe@N-C-x}$ were also evaluated. Moreover, we also assessed the treatment efficacy of the $\text{Fe}_3\text{C}/\text{Fe@N-C-x}$ catalysts on actual pharmaceutical wastewater samples. The corresponding achievements will be conducive to the development and application of MOF-derivatives in real wastewater decontamination.

2. Materials and methods

2.1. Fabrication of $\text{Fe}_3\text{C}/\text{Fe@N-C-x}$ catalysts

Firstly, MIL-88B(Fe) as the important precursor was prepared in terms of the previous study with slightly modification [24]. In short, 2.7 g $\text{FeCl}_3 \cdot 0.6\text{ H}_2\text{O}$ and 1.16 g terephthalic acid were spread in 50 mL of *N,N*-dimethylformamide. After that, the initial pH value was adjusted by adding 4 mL of NaOH solution (2 M) to the obtained suspension dropwise under continuous magnetic stirring for 30 min. Then the acquired suspension was encapsulated in a Teflon-lined stainless-steel autoclave and heated in an oven at $100\text{ }^\circ\text{C}$ for 720 min. After cooling to indoor temperature, the solids were gathered via centrifugation processing at 12,000 rpm for 5 min. Finally, the desired MIL-88B(Fe) powders were obtained after washing and vacuum drying processes.

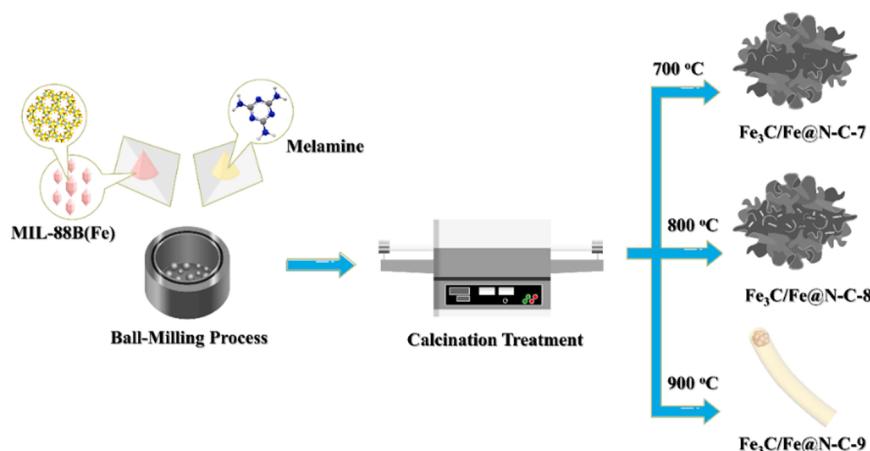
Secondly, the $\text{Fe}_3\text{C}/\text{Fe@N-C-x}$ catalysts were fabricated via a controlled method through calcinating the mixture of MIL-88B(Fe) and melamine, as illustrated in Scheme 1. In a standard procedure, 3 g melamine and 0.2 g MIL-88B(Fe) were mixed through a facile ball-milling processing. The operating parameters were set as 20 min and 30 Hz, respectively. Subsequently, the acquired precursors were transferred into a tubular furnace and heated at a pre-set temperature ranging from 700 to $900\text{ }^\circ\text{C}$ for 240 min at N_2 atmosphere with a heating rate of $5\text{ }^\circ\text{C}/\text{min}$. After the temperature decreased, the resulting solids were cleaned with $0.5\text{ mM H}_2\text{SO}_4$ for removing ferrous species on the carbon surface.

2.2. Procedure of catalytic degradation for organic pollutants

The initial concentration of sulfamethoxazole (SMX) was determined as 20 mg/L, the initial concentrations of rhodamine B (RhB), bisphenol A (BPA), tetracycline hydrochloride (TCH) and ciprofloxacin (CIP) were set as 10 mg/L. The dosage of $\text{Fe}_3\text{C}/\text{Fe@N-C-x}$ was 0.3 g/L. A specified volume of aqueous sample was retrieved at pre-set time intervals and immediately filtered through a $0.22\text{ }\mu\text{m}$ membrane. Heterogeneous catalytic degradation processes were initiated by adding PMS solution (250 mM, $20\text{ }\mu\text{L}$) into the reaction system. In the investigation of the influences of co-existing matters on the catalytic experiments, NaCl, Na_2SO_4 , NaHCO_3 , NaH_2PO_4 solutions with a concentration of 1 mM and humic acid (HA) solution with a concentration of 10 mg/L were introduced to the reaction solutions. The initial pH values of modeling pollutants were adjusted with addition of 0.1 mM HCl or NaOH. At each time intervals, the collected reaction solution must be added $10\text{ }\mu\text{L}$ MeOH to quench the different ROSs. With respect to reusability evaluation, the used catalysts can be easily separated from the reaction system with the aid of an external magnetic field. Then the retrieved solids were washed with ultrapure water for three times and dried at $60\text{ }^\circ\text{C}$ overnight for the subsequent catalytic experiment. All the experimental procedures were conducted at room temperature in a magnetic stirred reactor.

2.3. Analytical methods

The contents of SMX and BPA were detected by a VH-D10-A Thermo Scientific high performance liquid chromatograph (HPLC) equipped with a InertSustain® C-18 column ($2.1\text{ mm} \times 250\text{ mm}$, $5.0\text{ }\mu\text{m}$). The UV detection wavelengths were 270 and 227 nm, respectively. The mobile phases were acetonitrile/phosphoric acid (45:55, v/v) and acetonitrile/water (50:50, v/v), respectively. The corresponding flow rates were operated as 0.8 and $0.4\text{ mL}/\text{min}$, respectively. The contents of RhB, CIP



Scheme 1. Schematic illustration of the fabrication procedure of the magnetic $\text{Fe}_3\text{C}/\text{Fe@N-C-x}$.

and TCH were tested through a PerkinElmer Lambda 650 S UV–vis spectrophotometer. According to the previous reports, the corresponding maximum absorption wavelengths were located at 554, 276 and 357 nm, respectively [25]. The total organic carbon (TOC) concentrations of the untreated and catalytically degraded samples were determined by a Jena Multi N/C 3100 analyzer. The excitation-emission matrix (EEM) fluorescence spectra of the pharmaceutical wastewater samples were recorded on a Hitachi F-7000 fluorescence spectrophotometer. The background concentrations of inorganic ions in real pharmaceutical wastewater were measured by ICS-1500 and ICS-2100 ion chromatographic instruments. Chemical oxygen demand (COD) was determined by a Lianhua 5B-3 C (V7) speedy testing instrument. The organic components in actual pharmaceutical wastewater were extracted and analyzed according to the Method 1694 proclaimed by U.S. Environmental Protection Agency (EPA).

2.4. Mechanism study

Different quenching agents, such as methanol (MeOH: 1, 10 and 100 mM), tert-butanol (TBA: 1, 10 and 100 mM), *p*-benzoquinone (*p*-BQ: 1, 10 and 100 mM), L-histidine (1, 10 and 100 mM), dimethyl sulfoxide (DMSO: 1, 10 and 100 mM) and oxalate (1, 2 and 4 mM) were used to evaluate the contributions of $\text{SO}_4^{\cdot-}$, $\cdot\text{OH}$, $\cdot\text{O}_2^-$, $^1\text{O}_2$ and high-valent Fe species (HV-Fe) to catalytic degradation of organic pollutants, respectively. Furthermore, some ROSs were also detected by a JEOL JES-FA200 electron spin resonance (ESR) spectroscopy with 2,2,6,6-tetramethyl-4-piperidone (TEMP) and 5,5-dimethyl-1-pyrroline-*N*-oxide (DMPO) as trapping agents in phosphate buffer solution (pH = 7.4). Electrochemical tests including electrochemical impedance spectra (EIS), current response curves and linear sweep voltammetry (LSV) were conducted on a Metrohm Autolab PGSTAT204 electrochemical workstation.

2.5. Data analysis

To monitor the catalytic degradation efficiency of pharmaceutical wastewater more accurately, the EEMs data in the two triangle regions ($E_m \leq E_x + 20$ nm and $E_m \geq E_x - 10$ nm) were underwent zero setting process and the background spectrum of ultrapure water was deducted to remove Rayleigh and Raman scatterings [26]. The degradation kinetic curves of specific model pollutants were fitted using the pseudo-first-order kinetic model, as expressed as Eq. (1):

$$\ln(C_0/C_t) = -kt \quad (1)$$

where C_0 and C_t represented the concentrations of organic pollutants at the initial state and at degradation time t (min), respectively, k was the

degradation rate constant. All the catalytic experimental data were analyzed using Origin 2018.

3. Results and discussion

3.1. Characterization of as-prepared catalysts

3.1.1. Phase structure and textural properties

The powder X-ray diffraction (PXRD) patterns of the as-prepared MIL-88B(Fe) and $\text{Fe}_3\text{C}/\text{Fe@N-C-x}$ catalysts were displayed in Figs. S1 and 1(a). The pure MIL-88B(Fe) showed a sequence of diffraction peaks, which matched well with that of reported MIL-88B(Fe) structure, indicating the successful fabrication of MIL-88B(Fe) [34]. All the $\text{Fe}_3\text{C}/\text{Fe@N-C-x}$ catalysts exhibited an evident peak at $2\theta = 26.5^\circ$, which should be indexed to the (0 0 2) lattice plane of graphitic carbon (JCPDS No. 08-0415). Moreover, the diffraction peak at 26.5° became stronger and sharper with increasing of calcination temperature, indicating that elevated temperature can contribute to enhance the graphitization degree of $\text{Fe}_3\text{C}/\text{Fe@N-C-x}$ catalysts [27]. Furthermore, the strong peaks at $2\theta = 45.3^\circ$, 65.0° and 82.1° were detected in the patterns of $\text{Fe}_3\text{C}/\text{Fe@N-C-7}$, $\text{Fe}_3\text{C}/\text{Fe@N-C-8}$ and $\text{Fe}_3\text{C}/\text{Fe@N-C-9}$, which were belonged to the (1 1 0), (2 0 0) and (2 1 1) crystallographic planes of FNPs (JCPDS No. 870722), respectively [28]. And the diffraction peaks at 37.6° , 42.8° , 43.6° , 45.9° and 49.1° were assigned to the (0 2 1), (1 2 1), (2 1 0), (1 1 2) and (2 2 1) crystalline planes of Fe_3C components (JCPDS No. 892867) [29]. Additionally, the characteristic peaks originated from ferric oxides cannot be detected, reflecting that Fe^0 or Fe_3C particles were the dominant species and they might be dispersed in graphitic structures.

The functional groups in $\text{Fe}_3\text{C}/\text{Fe@N-C-x}$ were further monitored by Fourier transform infrared (FTIR), as depicted in Fig. 1(b). The wide and intense peak at 3410 cm^{-1} can be indexed to the O–H vibration generated by free or bound water molecules [5]. And the peak at 1600 cm^{-1} should be identified as the C=O stretching and aromatic skeletal vibration [30]. The other characteristic peak at 1052 cm^{-1} was referred to the stretching vibration of C–O functional group [31]. It was a remarkable fact that two characteristic peaks at 1543 and 590 cm^{-1} can be detected in the spectra of $\text{Fe}_3\text{C}/\text{Fe@N-C-x}$ samples, which were ascribed to C–N and Fe–N groups [31,32], indicating that N-doped structures (e.g., graphitic-N, pyridinic-N and pyrrolic-N) and Fe–N_x moiety might be formed in the carbonous skeleton.

Raman spectra of the $\text{Fe}_3\text{C}/\text{Fe@N-C-x}$ materials were depicted in Fig. 1(c) to investigate the structural features and graphitization degree. Typically, the defective level of a carbonaceous sample can be expressed by the intensity ratio of the D band ($\sim 1350\text{ cm}^{-1}$) to G band ($\sim 1588\text{ cm}^{-1}$) (I_D/I_G) [17]. The D band was related to the amorphous

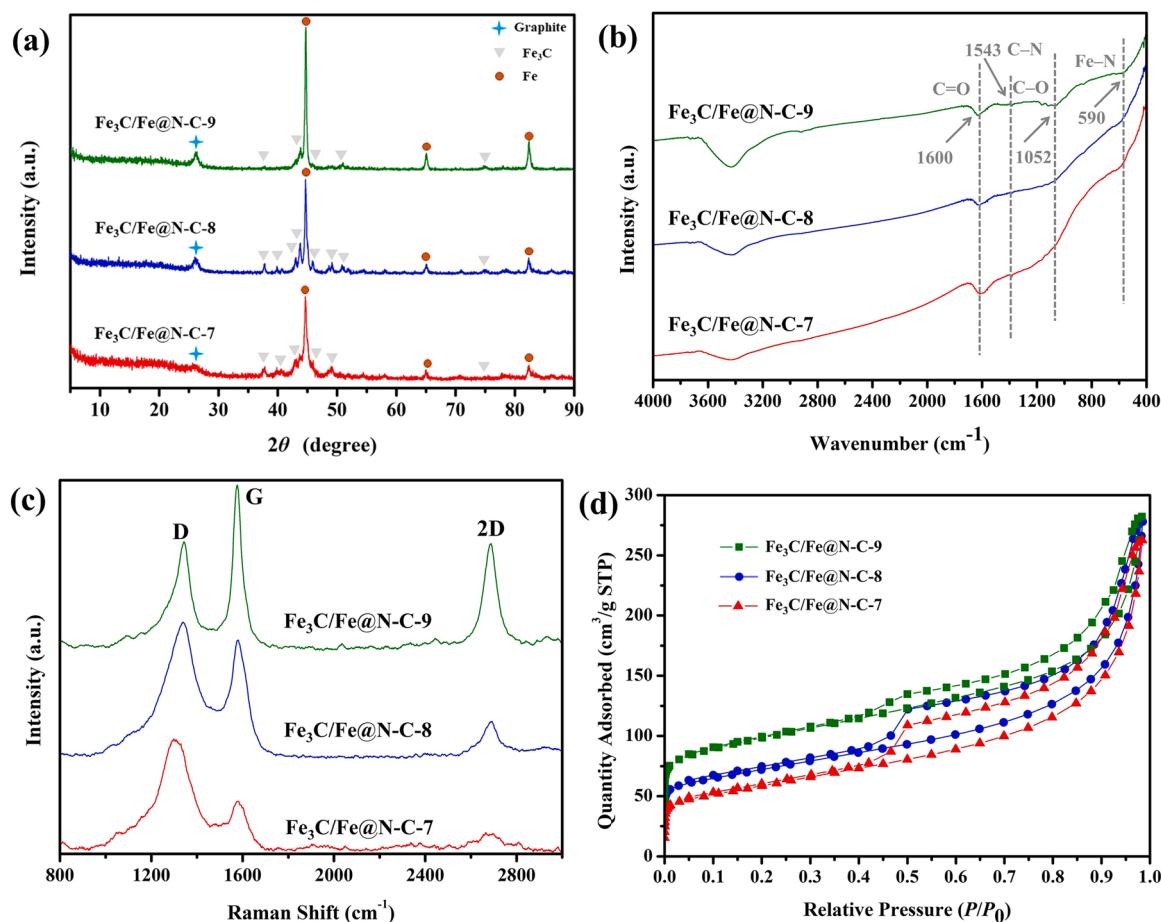


Fig. 1. (a) PXRD patterns, (b) FTIR spectra, (c) Raman spectra and (d) N₂ adsorption-desorption isotherms of the as-fabricated Fe₃C/Fe@N-C-x catalysts.

carbon layers, disorders, edges and boundaries of the sp^3 defects, whereas the G band was assigned to the E_{2g} vibration originated from sp^2 -hybridized graphite carbon. Therefore, as the ratio of I_D/I_G went up, the defect degree increased, whereas the degree of graphitization decreased [33]. The I_D/I_G value was estimated as 1.86 for Fe₃C/Fe@N-C-7, which decreased with the calcination temperature. And the I_D/I_G value dropped to 0.79 for Fe₃C/Fe@N-C-9, indicating that Fe₃C/Fe@N-C-9 possessed the strongest sp^2 -hybridized structure and minimum defects among all catalysts. The above physicochemical properties might endow the Fe₃C/Fe@N-C-9 have greater electrical conductivity and adsorption capacity for organic pollutants via π - π interaction. Additionally, a 2D peak located at 2705 cm⁻¹ as the other characteristic signal of graphitic material can be clearly detected in the Raman spectrum [34]. The intense peak appeared in each Fe₃C/Fe@N-C-x catalyst implied the presence of few-layer structures. Combining with PXRD and Raman analysis, it can be inferred that higher calcination temperature could enhance the corresponding graphitization degree.

Fig. 1(d) showed the N₂ adsorption-desorption isotherms of the Fe₃C/Fe@N-C-x catalysts. The Brunauer-Emmett-Teller (BET) specific surface areas of the Fe₃C/Fe@N-C-7, Fe₃C/Fe@N-C-8 and Fe₃C/Fe@N-C-9 were 173.55, 209.19 and 254.99 m²/g, respectively. Furthermore, the N₂ adsorption-desorption isotherm displayed a typical type-IV with an H₄-type hysteresis loop at a relative pressure (P/P_0) of 0.5–1.0, revealing that a mixture of microporous and mesoporous architecture in Fe₃C/Fe@N-C-x [35]. Moreover, the Barrett-Joyner-Halenda (BJH) pore size distribution curves of the Fe₃C/Fe@N-C-x catalysts were shown in Fig. S2. It was obvious that most of pores possessed widths in the range of 1–50 nm, and the above three catalysts had peaks at about 2 nm, indicating that the as-prepared Fe₃C/Fe@N-C-7, Fe₃C/Fe@N-C-8 and

Fe₃C/Fe@N-C-9 had micropores as well as mesopores. They were in line with the results obtained by N₂ adsorption-desorption isotherms. In general, the calcination of MIL-88B(Fe) and melamine hybrids allowed the Fe₃C/Fe@N-C-x materials to have larger specific surface areas and richer porous structure, leading to the adsorption and transfer of PMS, and organic pollutants could be enhanced during the heterogeneous catalytic process.

3.1.2. Morphological analysis

The morphologies and microstructures of the as-fabricated catalysts were observed by scanning electron microscopy (SEM) and high-resolution transmission electron microscopy (HRTEM) instruments, and the corresponding micrographs were exhibited in Fig. 2 and S3. Fig. S3 showed that the pure MIL-88B(Fe) possessed a hexagonal microrod morphology, which was in line with our reported work [34]. As revealed in Fig. 2(a), the Fe₃C/Fe@N-C-7 exhibited the lettuce-like structure with a rough surface and an average size of 2–3 μ m. It could be attributed to that the decomposition of melamine at high temperature will instantaneously release NH₃ [36], which was inclined to tailor the porous structure and surface chemistry of MIL-88B(Fe)-graphitized carbonaceous material. When the calcination temperature rose to 800 °C, a few of carbon nanotubes were formed and they were wrapped in the lettuce-like structure (Fig. 2(b)). However, after thermal pyrolysis at 900 °C, the lettuce-like structure disappeared and only regularly tubing structures with dimensions of 0.5–1.5 μ m in length were observed in the SEM micrograph of Fe₃C/Fe@N-C-9 (Fig. 2(c)), which was mainly due to the hybrid of melamine and MIL-88B(Fe) was fully converted to the graphitic structures and Fe³⁺/Fe²⁺ embedded within MIL-88B(Fe) was inclined to transform into iron carbide and zero-valent Fe particles under N₂ atmosphere, this result can also be proved by PXRD

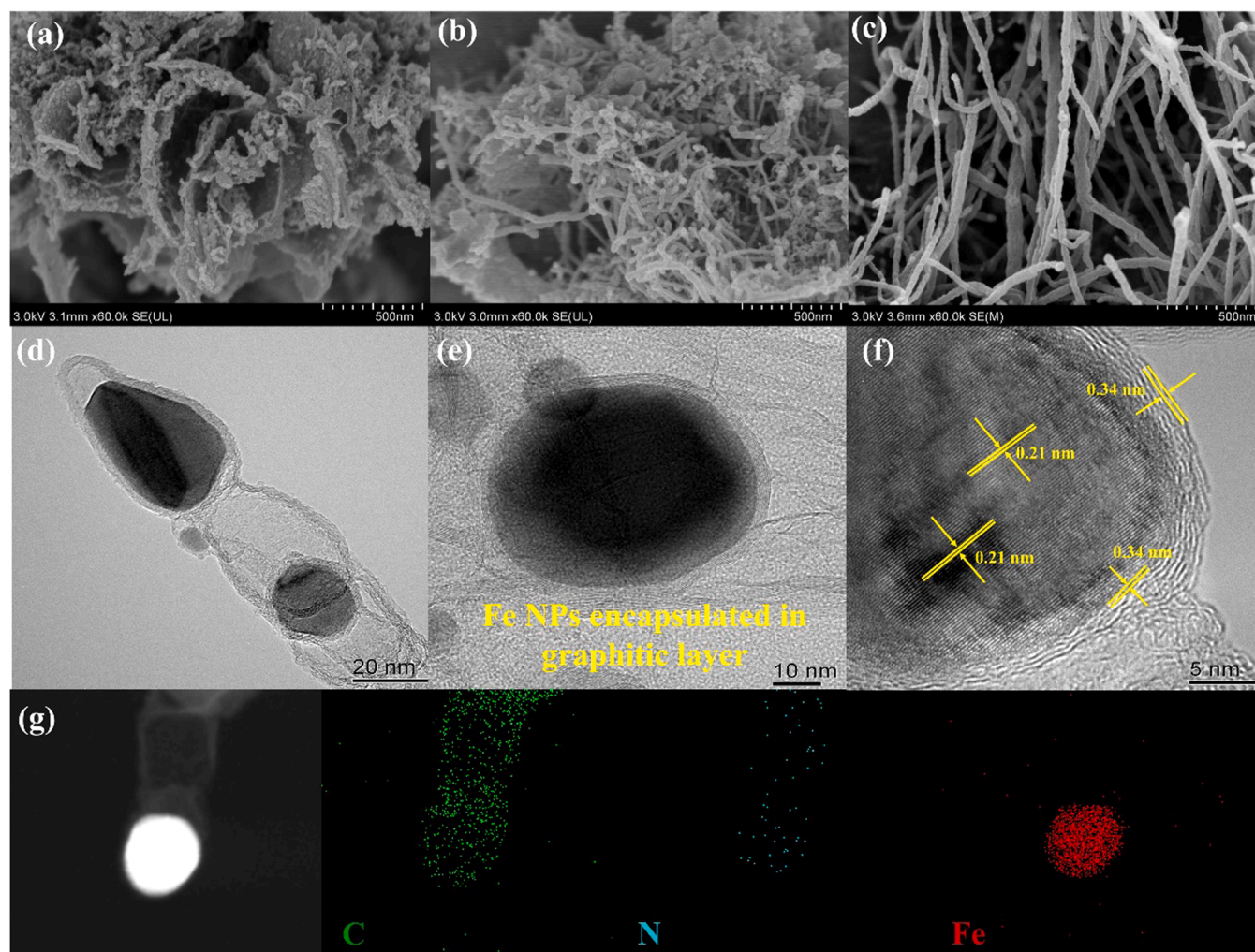


Fig. 2. SEM micrographs of (a) $\text{Fe}_3\text{C}/\text{Fe}@N\text{-C-7}$, (b) $\text{Fe}_3\text{C}/\text{Fe}@N\text{-C-8}$, (c) $\text{Fe}_3\text{C}/\text{Fe}@N\text{-C-9}$, (d)–(f) HRTEM micrographs of $\text{Fe}_3\text{C}/\text{Fe}@N\text{-C-9}$ and (g) TEM elemental mappings of C, N and Fe.

results. According to the previous studies [37,38], gasification, nucleation, migration and generation were the main formation process of CNTs. As to $\text{Fe}_3\text{C}/\text{Fe}@N\text{-C-9}$, the growth of tubular morphology followed a decomposition-reconstruction mechanism, in which melamine precursor would gasify during pyrolysis and then was transformed into CNTs. As the calcination temperature increased to 900 °C, melamine would totally decompose into small gaseous molecules like NH_3 , which could be permeated into MIL-88B(Fe) spindles. Finally, ferrous cations were reduced to metal nanoparticles, which could be used as catalysts to facilitate the formation of tubular structures. As a result, the $\text{Fe}_3\text{C}/\text{Fe}@N\text{-C-9}$ was obtained.

More interestingly, from the HRTEM micrographs of $\text{Fe}_3\text{C}/\text{Fe}@N\text{-C-9}$ (Fig. 2(d)–(f)), the uniform distribution and encapsulation of a number of dark-contrast nanoparticles with an average size of 20–55 nm beneath the well-defined carbonaceous shells can be clearly found. The HRTEM micrograph in Fig. 2(f) presented a *d*-spacing of crystalline lattice with 0.21 nm, which corresponded to the (2 1 1) crystallographic plane of Fe_3C component [28]. Furthermore, the lattice spacing of outer spheres was 0.34 nm, which was related to the (0 0 2) plane of graphite carbon [39]. This experimental result was also consistent with PXRD and Raman analysis. Meanwhile, TEM elemental distribution mapping (Fig. 2(g)) showed that N element was homogeneously distributed on the carbon layers and Fe nanoparticles were wrapped tightly by N-doped carbon nanotubes (NCNTs). These fascinating features might protect Fe species from leaching during the catalytic process and could improve the

catalytic efficiency.

3.1.3. Surface chemical analysis

The chemical compositions and surface chemical states of $\text{Fe}_3\text{C}/\text{Fe}@N\text{-C-x}$ samples were analyzed using X-ray photoelectron spectroscopy (XPS). Four core elements including C, O, N and Fe were identified from the XPS survey spectra in Fig. S4. On the basis of the integrated peak areas, the atomic ratios of C, O, N and Fe on the surfaces of $\text{Fe}_3\text{C}/\text{Fe}@N\text{-C-7}$, $\text{Fe}_3\text{C}/\text{Fe}@N\text{-C-8}$ and $\text{Fe}_3\text{C}/\text{Fe}@N\text{-C-9}$ were listed in Table S1. It can be found that the atomic percentages of C increased with the increasing calcination temperatures. However, the atomic percentages of N and Fe were trending in the opposite direction. In the high-resolution C 1s spectra of various $\text{Fe}_3\text{C}/\text{Fe}@N\text{-C-x}$ samples (Fig. 3(a)), the characteristic peaks at 284.8, 285.2, 287.0 and 288.7 eV were ascribed to sp^2 graphitic-C ($C-\pi$), $C=N$, Fe_3C and $C-N$ structures, respectively [40]. The O 1s spectra can be split into four peaks centered at 530.5, 531.4, 532.2 and 533.6 eV, which were indexed to $C=O$, $C-O$, $C-C=O$ and $O-C=O$ groups, respectively [17,40]. High-resolution N 1s spectra could be well deconvoluted into five peaks with binding energies of 398.1, 398.9, 400.1, 401.3 and 403.7 eV, corresponding to pyridinic-N, $Fe-N_x$, pyrrolic-N, graphitic-N and oxidized-N species, respectively [41,42]. Previous reports suggested that the N heteroatoms existed in the carbon-based catalysts, particularly the graphitic, pyrrolic and pyridinic N, can be deemed as Lewis basic sites to facilitate the PMS adsorption and electron-transfer reaction via manipulating the

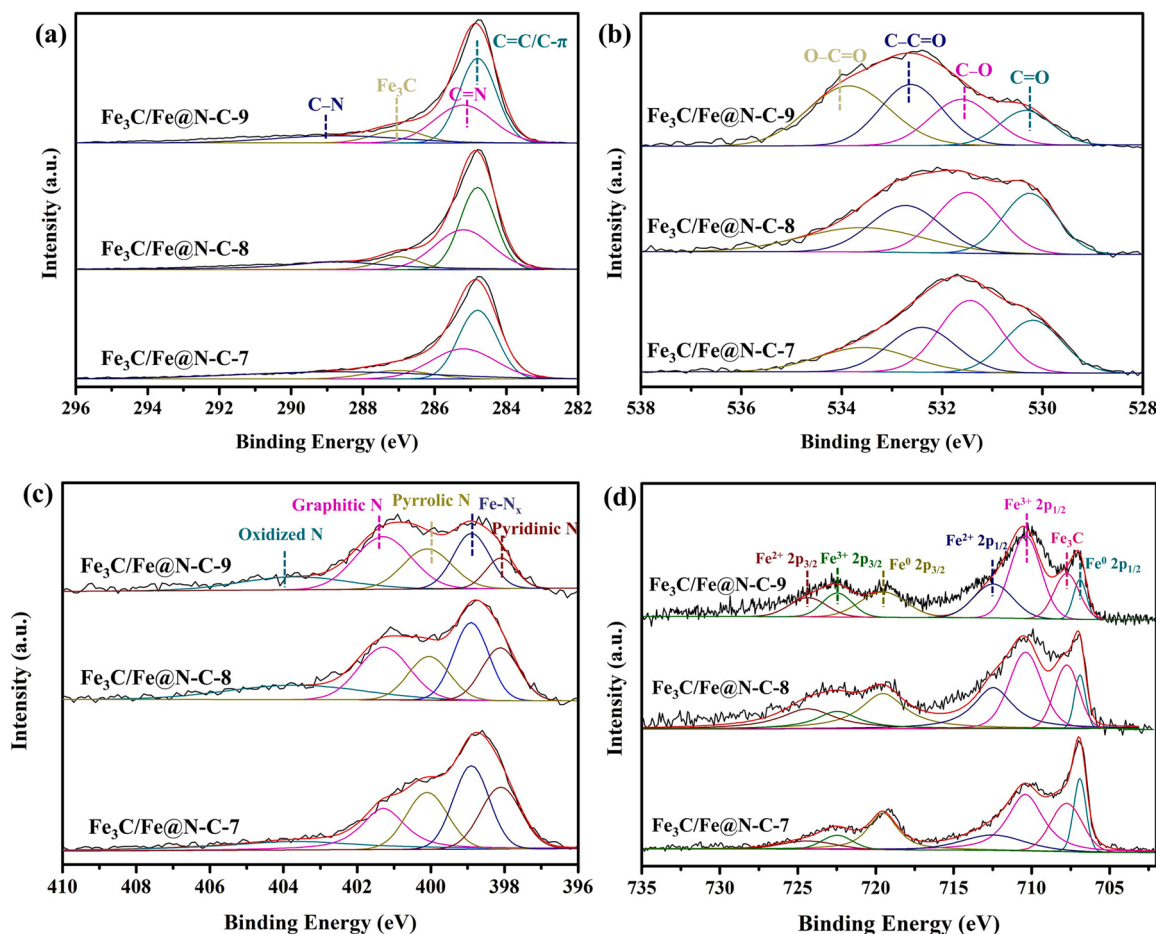


Fig. 3. XPS spectra of (a) C 1s, (b) O 1s, (c) N 1s and (d) Fe 2p in $\text{Fe}_3\text{C}/\text{Fe@N-C-x}$ catalysts.

neighboring carbon atoms to be positively charged [43]. Besides, the Fe-N_x coordination moieties were also detected, which confirmed the FTIR results. And it was qualified for acting as redox active sites for activating PMS during heterogeneous catalytic degradation [44,45]. Thus, the presence of above N species was expected to enhance the electron transportation capability, leading to boost the catalytic degradation performances for organic pollutants. Additionally, the Fe 2p spectra of $\text{Fe}_3\text{C}/\text{Fe@N-C-x}$ samples can be disintegrated into seven peaks at 707.2, 720.6, 710.9, 723.7, 713.1, 725.7 and 708.1 eV, which should be indexed to Fe^0 2p_{1/2}, Fe^0 2p_{3/2}, Fe^{3+} 2p_{1/2}, Fe^{3+} 2p_{3/2}, Fe^{2+} 2p_{1/2}, Fe^{2+} 2p_{3/2} spin orbitals and Fe_3C species, respectively.

As different active sites possess great impacts on the pathway and efficacy of PMS activation, therefore the potential active sites and their relative contents were summarized in Table 1. Firstly, the contents of C- π moieties increased from 700 °C to 900 °C, and $\text{Fe}_3\text{C}/\text{Fe@N-C-9}$ possessed the maximum percentage of 40.4% in comparison with other

catalysts. As Duan and co-workers [46,47] suggested that the asymmetric O-O bond in PMS molecules (HO-SO_4^-) was prone to interact and weaken by sp^2 -hybridized carbonaceous network with conjugated π structures, thereby more available C- π moieties may endow $\text{Fe}_3\text{C}/\text{Fe@N-C-9}$ with improved catalytic activity. Recently, it was demonstrated that C=O and O-C=O groups can function as active sites for the production of $^1\text{O}_2$ via PMS activation process [17,47]. In this work, the amount of O-C=O boosted from 1.02% ($\text{Fe}_3\text{C}/\text{Fe@N-C-7}$) to 2.12% ($\text{Fe}_3\text{C}/\text{Fe@N-C-9}$) and that of C=O reduced from 1.37% ($\text{Fe}_3\text{C}/\text{Fe@N-C-7}$) to 0.78% ($\text{Fe}_3\text{C}/\text{Fe@N-C-9}$). But the total amount of O-C=O and C=O species did increase with calcination temperatures (from 2.39% to 2.90%). Therefore, it was rational to infer that the O-C=O and C=O formed in $\text{Fe}_3\text{C}/\text{Fe@N-C-9}$ might activate PMS and generate more $^1\text{O}_2$ during the catalytic process. In terms of Fe^0 , the corresponding content dropped to 0.17% in $\text{Fe}_3\text{C}/\text{Fe@N-C-9}$. Although the relative amounts of graphitic N, pyridinic N, pyrrolic N, and Fe-N_x decreased with the calcination temperature rising from 700 to 900 °C, the presence of above N-doped species may synergistically reinforce the catalytic activity for organic pollutants degradation via a “donor-acceptor complex” mechanism [16].

3.1.4. ^{57}Fe Mössbauer spectrum analysis

In order to further confirm the iron species in $\text{Fe}_3\text{C}/\text{Fe@N-C-9}$, the ^{57}Fe Mössbauer spectrum was also conducted. As illustrated in Fig. 4, the spectrum can be fitted with three doublets and three sextets. The parameters including magnetic hyperfine field (B_{hf}), isomer shift (δ), quadrupole shift (ϵ), full width at half maxima (FWHM) and the relative content were shown in Table 2. According to the detailed analysis, the doublets 1–3 were assigned to $\text{Fe}^{\text{II}}\text{N}_4$ (low spin), $\text{Fe}^{\text{II}}\text{N}_4$ (medium spin)

Table 1

Relative contents (%) of potential active sites for PMS activation in $\text{Fe}_3\text{C}/\text{Fe@N-C-x}$.

Species	$\text{Fe}_3\text{C}/\text{Fe@N-C-7}$	$\text{Fe}_3\text{C}/\text{Fe@N-C-8}$	$\text{Fe}_3\text{C}/\text{Fe@N-C-9}$
C- π	32.5	35.8	40.4
O-C=O	1.02	1.35	2.12
C=O	1.37	1.40	0.78
Graphitic N	2.27	1.59	1.67
Pyridinic N	2.32	1.16	0.49
Pyrrolic N	2.23	1.07	1.04
Fe-N_x	2.77	1.63	1.11
Fe^0	0.79	0.25	0.17

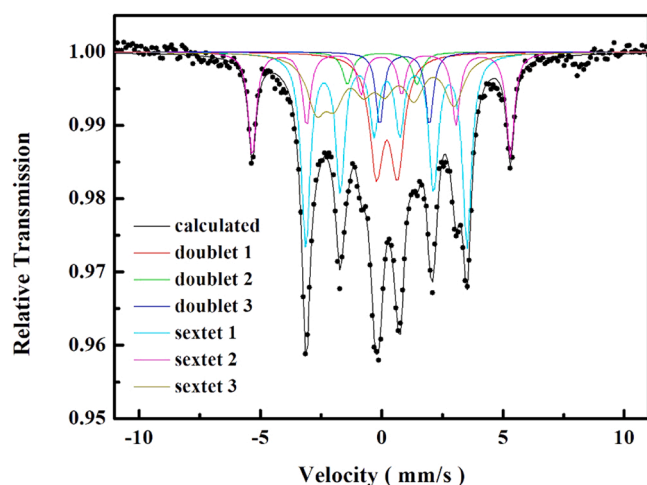


Fig. 4. ^{57}Fe Mössbauer spectrum of $\text{Fe}_3\text{C}/\text{Fe@N-C-9}$.

Table 2

Mössbauer parameters at 298 K for the spectrum of the $\text{Fe}_3\text{C}/\text{Fe@N-C-9}$.

Component	B_{hf} (T)	δ (mm/s)	ϵ (mm/s)	FWHM (mm/s)	Content (%)
Doublet 1	—	0.22	0.86	0.34	15.5
Doublet 2	—	0.03	2.87	0.23	3.1
Doublet 3	—	0.95	2.05	0.18	5.5
Sextet 1	205.95	0.21	0.02	0.22	36.1
Sextet 2	329.42	-0.01	0	0.2	17.2
Sextet 3	175.81	-0.08	-0.45	0.47	22.6

and $\text{N-Fe}^{\text{II}}\text{N}_{2+2}$ (high spin), while those of sextets were in accordance with Fe_3C , $\alpha\text{-Fe}$ and $\text{Fe}_{2.2}\text{C}$, respectively [27,48]. This result indicated that the as-prepared $\text{Fe}_3\text{C}/\text{Fe@N-C-9}$ was composed of iron carbide with the balance remaining in $\alpha\text{-Fe}$ and Fe-N_4 , affirming the PXRD, HRTEM and XPS analysis. With this clarification, it was clear that the formation of Fe_3C and $\alpha\text{-Fe}$ species endowed $\text{Fe}_3\text{C}/\text{Fe@N-C-9}$ with ferromagnetic property.

3.2. Catalytic activities of $\text{Fe}_3\text{C}/\text{Fe@N-C-x}$ for PMS activation

3.2.1. Organic pollutants degradation by $\text{Fe}_3\text{C}/\text{Fe@N-C-x}$

As a normally persistent and hydrophobic antibiotic that is continually detected in various water environments with high concentration of mg/L level [49], SMX was firstly selected as the modeling pollutant to assess the catalytic activities of the $\text{Fe}_3\text{C}/\text{Fe@N-C-x}$ samples. As exhibited in Fig. 5(a), it was clear that only 12.5% of SMX molecules were removed in 10 min with the absence of catalysts, implying that the oxidation capacity of PMS alone was very limited. Furthermore, each of the $\text{Fe}_3\text{C}/\text{Fe@N-C-x}$ materials possessed relatively high adsorption capacities for SMX without addition of PMS, approximately 32.2%, 41.2% and 49.9% of SMX was adsorbed by $\text{Fe}_3\text{C}/\text{Fe@N-C-7}$, $\text{Fe}_3\text{C}/\text{Fe@N-C-8}$ and $\text{Fe}_3\text{C}/\text{Fe@N-C-9}$, respectively. Their prominent adsorption capacities were mainly due to the tailored surface chemistry and hierarchical porous structure. During the pyrolysis transformation process, the original skeleton structure of MIL-88B(Fe) orderly collapsed and ferrous species tended to agglomerate. Therefore, after washing by H_2SO_4 solution, the accessible FNPs covered on the surface of the prepared catalysts can be removed and the occupied active sites were simultaneously released. Hence more exposed surface and available active sites should be contributed to adsorption process. More importantly, as the calcination temperatures increased from 700 to 900 °C, the reason for the gradual increase in adsorption efficiency was formation of more sp^2 -hybridized structures ($\text{C-}\pi$ species) in $\text{Fe}_3\text{C}/\text{Fe@N-C-9}$. The larger specific surface area ($254.99\text{ m}^2/\text{g}$) and stronger π - π interactions between the carbon layers of $\text{Fe}_3\text{C}/\text{Fe@N-C-9}$ and SMX molecules

endowed its highest adsorption capacity [16,50]. And the ameliorative adsorption performance will eventually facilitate the rapid decontamination of SMX from wastewater.

Being compared to adsorption processes in darkness conditions, when the PMS was introduced, the decomposition of SMX can be regarded as a two-stage-reaction. In the first stage, $\text{Fe}_3\text{C}/\text{Fe@N-C-7}$, $\text{Fe}_3\text{C}/\text{Fe@N-C-8}$ and $\text{Fe}_3\text{C}/\text{Fe@N-C-9}$ exhibited ultrafast kinetics for eliminating SMX molecules with removal efficiencies of 83.4%, 89.4% and 94.1%, respectively. For comparison, MIL-88B(Fe) was employed as reference for the catalytic reaction under the identical conditions. As shown in Fig. S5, MIL-88B(Fe) alone exhibited negligible catalytic activity. While MIL-88B(Fe) + PMS system just led to 32.0% of SMX removal within 10 min. They were far less than the efficiencies achieved by the $\text{Fe}_3\text{C}/\text{Fe@N-C-x}$ catalysts, elucidating that the as-prepared $\text{Fe}_3\text{C}/\text{Fe@N-C-x}$ were the most efficient catalyst among them. Moreover, to ascertain the role of MIL-88B(Fe), a control experiment by calcinating the physical mixture of melamine and the precursors of MIL-88B(Fe) ($\text{FeCl}_3 \cdot 0.6\text{ H}_2\text{O}$ and terephthalic acid) was carried out. The as-fabricated material named P-9 was characterized by PXRD, SEM as well as HRTEM. And the corresponding catalytic activity toward SMX was investigated. As shown in Fig. S6(a), the P-9 displayed stronger graphite characteristic peak at $2\theta = 26.5^\circ$. However, from its SEM and HRTEM images (Fig. S6(b)-(c)), plicated and stacked carbon layer structures were observed, in which morphology of carbon nanotubes had almost disappeared. More importantly, a much lower catalytic efficiency toward SMX was detected as compared to that of $\text{Fe}_3\text{C}/\text{Fe@N-C-9}$. The above result revealed that the ordered distribution of ferrous species in MOFs was essential for the synthesis of even-distributed FNPs wrapped in CNT structures.

To deeply explore the catalytic activities of the $\text{Fe}_3\text{C}/\text{Fe@N-C-x}$, the pseudo-first-order kinetic model was applied to express the degradation behaviors of SMX molecules over the $\text{Fe}_3\text{C}/\text{Fe@N-C-x}$ catalysts. As illustrated in Fig. 5(b), the degradation rate constant (k_1) acquired by the $\text{Fe}_3\text{C}/\text{Fe@N-C-9}$ + PMS system in the initial stage reached to $2.84 \pm 0.22735\text{ min}^{-1}$, which was about 1.58 and 1.26 times higher than those for $\text{Fe}_3\text{C}/\text{Fe@N-C-7}$ ($1.80 \pm 0.06364\text{ min}^{-1}$) and $\text{Fe}_3\text{C}/\text{Fe@N-C-8}$ ($2.25 \pm 0.12873\text{ min}^{-1}$), respectively. Furthermore, as depicted in Fig. S7, the oxidation rate constants obtained in the second stage (k_2) were relatively sluggish, in which k_2 values were calculated to be 0.01 ± 0.00078 , 0.02 ± 0.00639 and $0.50 \pm 0.01757\text{ min}^{-1}$ for $\text{Fe}_3\text{C}/\text{Fe@N-C-7}$, $\text{Fe}_3\text{C}/\text{Fe@N-C-8}$ and $\text{Fe}_3\text{C}/\text{Fe@N-C-9}$, respectively. The corresponding mechanism would be further elaborated later in this study.

These experimental results suggested that the calcination temperature not only seriously affected the morphologies of the $\text{Fe}_3\text{C}/\text{Fe@N-C-x}$, but also strongly affected their PMS activation efficiencies. More importantly, it was worth noting that the k values obtained in the first stage were correlated well to the relative contents of $\text{C-}\pi$, algebraic sum of O-C=O and C=O (as depicted in Fig. 5(c)). The corresponding correlation coefficients (r^2) were 0.99 and 0.81, respectively. Interestingly, previous studies had proved that the sp^2 -hybridized N-doping species including graphitic N, pyridinic N, pyrrolic N and Fe-N_x sites played significant roles in activating PMS [12,51,52]. Nonetheless, we found a negative correlation between the k_1 values and the amount of total N species (Fig. 5(d)). Therefore, the above experimental phenomena indicated that the graphite carbon component and the co-existence of oxygen-containing groups such as O-C=O and C=O were the dominant forces for ultrafast catalytic degradation of SMX.

Meanwhile, it was not difficult to see that the degradation of SMX encountered the second stages over the as-prepared $\text{Fe}_3\text{C}/\text{Fe@N-C-x}$ materials, especially for the optimum $\text{Fe}_3\text{C}/\text{Fe@N-C-9}$, the residual SMX molecules in reaction system can be completely removed. This might be attributed to the synergism of encapsulation of FNPs and N-doping species further enhanced the catalytic activities via tuning the electron properties of the carbonaceous materials. For instance, the existence of carbon nanotube structures in $\text{Fe}_3\text{C}/\text{Fe@N-C-9}$ can confine the Fe_3C or Fe^0 nanoparticles, which can accelerate the electron transportation from

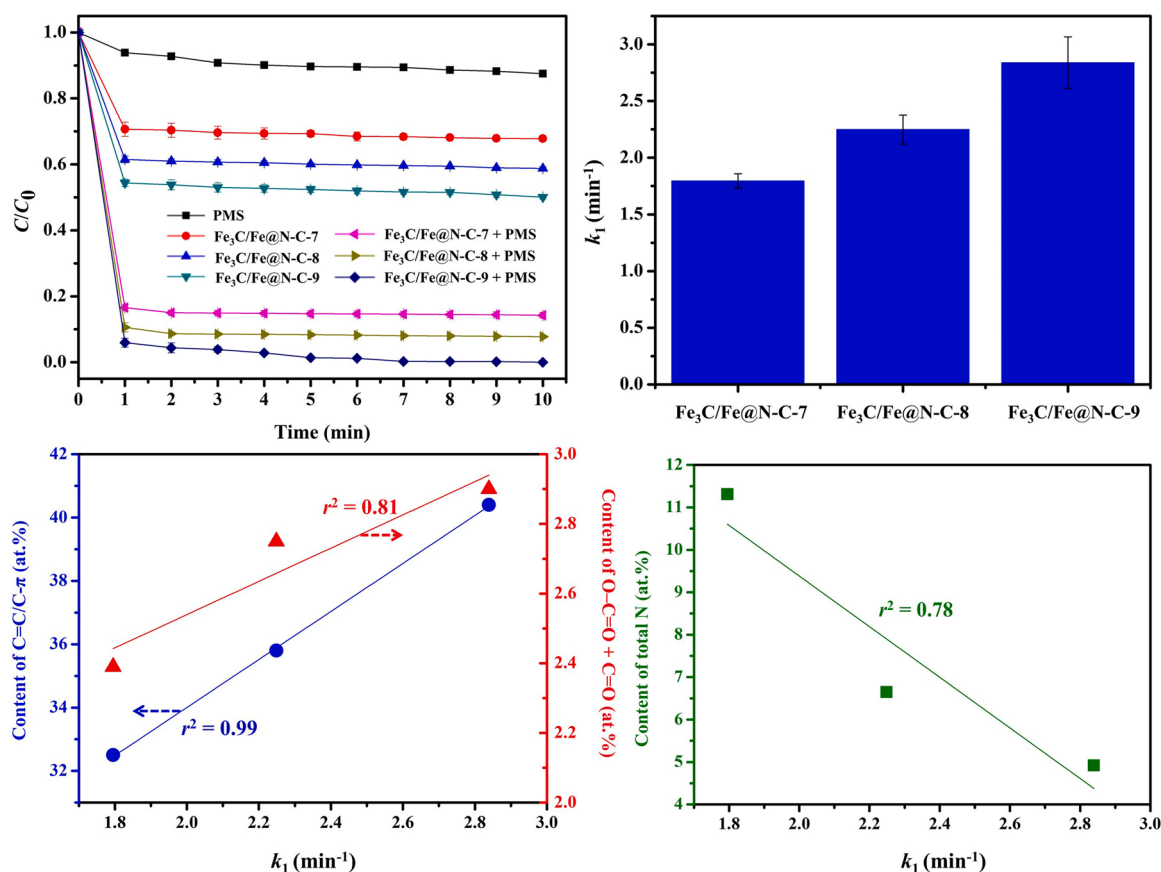


Fig. 5. (a) Catalytic degradation of SMX over various $\text{Fe}_3\text{C}/\text{Fe}@N\text{-C-}x$ catalysts, (b) the corresponding pseudo-first-order kinetic constants (k_1) obtained in the initial stage, (c-d) the apparent SMX removal rates as functions of the content of C- π , algebraic sum of O-C=O and C=O, total N elements. $[\text{PMS}]_0 = 0.1$ mM, $[\text{SMX}]_0 = 20$ mg/L, catalyst dosage = 0.3 g/L.

the ferrous components to the interacted carbon atoms, thereby enhancing the electron accumulation in specific carbon lattice for subsequent redox process [53]. Besides, the creation of N-dopants was beneficial to overcome the chemical inertness of graphitic lattice and gave rise to the neighboring carbon atoms being positively charged, further leading to more close interaction between the as-prepared catalysts and PMS to generate catalyst-PMS complexes [10,12]. Then, the electrons will be extracted from the vulnerable SMX molecules by the $\text{Fe}_3\text{C}/\text{Fe}@N\text{-C-}x\text{-PMS}^*$ complex for catalytic degradation process. Additionally, the co-existence of N-doping species can cooperatively promote the electron migration from FNPs to carbon atoms [54,55],

which was also conducive to improve catalytic efficiency. In addition, the PMS activation over $\text{Fe}_3\text{C}/\text{Fe}@N\text{-C-9}$ for the decomposition of SMX was compared with other reported heterogeneous catalytic materials (Table 3), showing that the as-prepared $\text{Fe}_3\text{C}/\text{Fe}@N\text{-C-9}$ can treat higher concentration of SMX with fastest reaction rate and lower consumption of PMS, thus the $\text{Fe}_3\text{C}/\text{Fe}@N\text{-C-9}$ possessed a stronger application potential.

3.2.2. Environmental factors on SMX degradation by $\text{Fe}_3\text{C}/\text{Fe}@N\text{-C-}x$

The influence of initial pH on SMX removal was investigated in the $\text{Fe}_3\text{C}/\text{Fe}@N\text{-C-9} + \text{PMS}$ reaction system. As shown in Fig. 6(a), the SMX

Table 3

Comparison of catalytic activation of PMS for SMX removal.

Catalyst	Dosage (g/L)	SMX concentration (mg/L)	PMS concentration (mM)	Energy source	Efficiency (%)	Reaction rate (min ⁻¹)	Reference
Co_3O_4 @NCNTs	0.01	10	1.19	Darkness	100	0.22	[56]
$\text{FeCo}_2\text{S}_4\text{-CN}$	0.02	4.98	0.15	Darkness	91.9	0.15	[57]
$\text{CuO}@Al_2\text{O}_3$	0.5	10	0.4	Darkness	99	N/A	[58]
$\text{CoFe}_2\text{O}_4\text{-EG}$	0.6	10	0.4	Darkness	100	0.18	[59]
$\text{FeO}_y/\text{S-g-C}_3\text{N}_4$	0.2	10	0.8	Darkness	100	0.06	[60]
Coconut-shell-derived biochar (CSBC)	0.15	12.66	0.6	Darkness	85	0.01	[61]
Dairy manure digestate derived biochar (DMDB)	1.00	15.00	2.50	Darkness	90.2	0.02	[62]
Cu-N-C	0.2	18	1.19	Darkness	100	0.16	[63]
$\text{Fe}_3\text{O}_4/\beta\text{-FeOOH}$	0.2	5	0.89	Darkness	91	0.08	[64]
$\text{CoAl-LDH}@CoFe\text{-PBA}$	0.1	10	0.3	Darkness	98	0.37	[65]
$\text{Fe-Co-O-g-C}_3\text{N}_4$	0.2	10	0.8	Darkness	100	0.09	[66]
$\text{g-C}_3\text{N}_4$	0.1	5	0.1	UV-A LED light	95	0.05	[67]
PDA-gCN-1.0	0.05	10	1	Darkness	100	1.70	[68]
$\text{Fe}_3\text{C}/\text{Fe}@N\text{-C-9}$	0.3	20	0.1	Darkness	100	2.84	This work

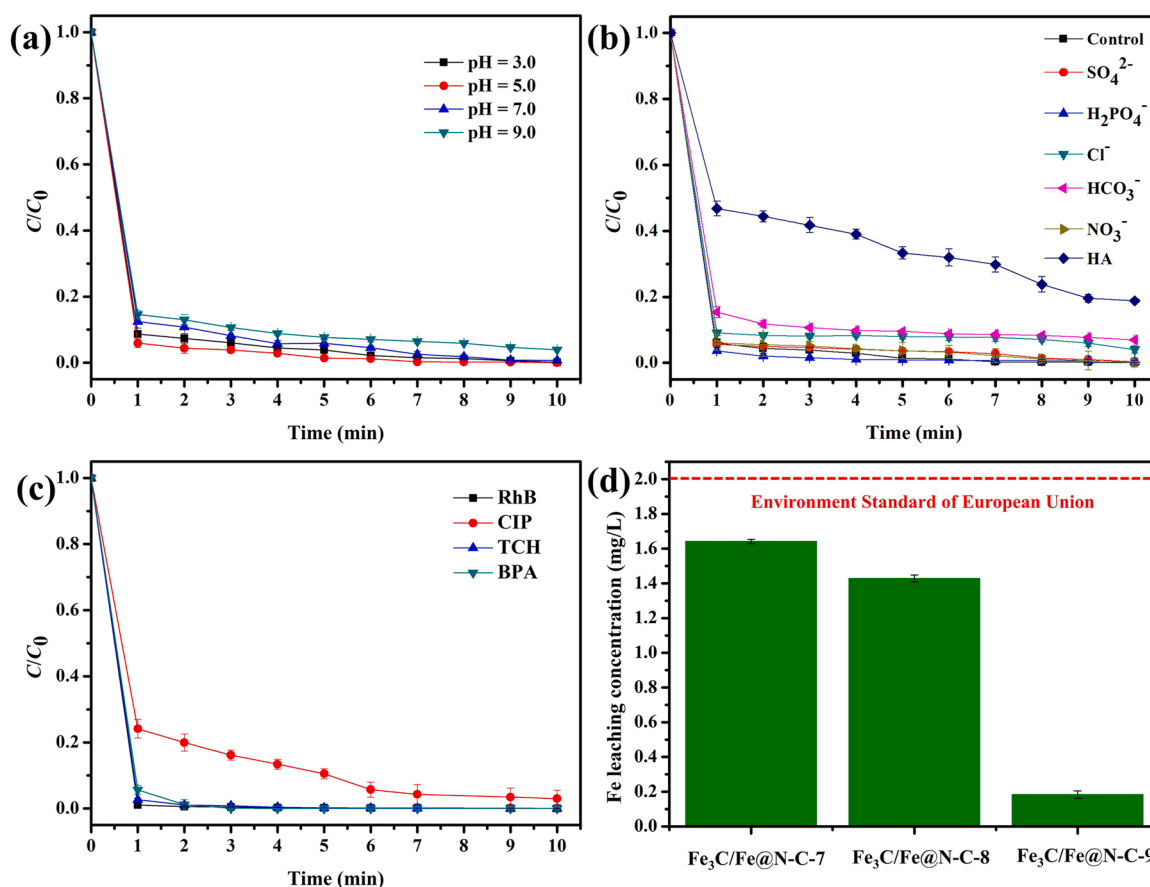


Fig. 6. SMX catalytic degradation under different experimental conditions: (a) pH, (b) the co-existence of inorganic anions and humic acid, (c) catalytic performances of different organic pollutants over the $Fe_3C/Fe@N-C-9$ and (d) Fe leaching from different $Fe_3C/Fe@N-C-x$ catalysts. $[PMS]_0 = 0.1$ mM, $[SMX]_0 = 20$ mg/L, $Fe_3C/Fe@N-C-9 = 0.3$ g/L, $[anions] = 1$ mM, $[HA]_0 = [RhB]_0 = [CIP]_0 = [TCH]_0 = [BPA]_0 = 10$ mg/L.

catalytic degradation rates at pH of 3.0, 5.0, 7.0 and 9.0 still maintained at relatively high levels ($1.92\text{--}2.84\text{ min}^{-1}$) and nearly all the SMX molecules were eliminated within 10 min. This result revealed that the constructed $Fe_3C/Fe@N-C-9 + PMS$ system can be applied to treat wastewater over a broad working pH (3.0–9.0). However, it was not difficult to observe that the SMX degradation rate slightly increased as pH values decreased, this increasement should be attributed to the surface attraction effect between $Fe_3C/Fe@N-C-9$ and PMS at lower pH values. Under the acidic conditions (pH = 3.0 or 5.0), the surface potentials of $Fe_3C/Fe@N-C-9$ were 4.65 and 9.62 mV, respectively (the zeta potential diagram of $Fe_3C/Fe@N-C-9$ was shown in Fig. S8), which would be conducive to attract HSO_5^- anions to trigger catalytic degradation process. Prior studies suggested that the reaction between PMS and N-doped active sites on the surface of carbonaceous materials was more favorable at lower pH conditions [69], thus the presence of N-doped species in $Fe_3C/Fe@N-C-9$ might facilitate the activation of PMS when pH being 3.0 and 5.0. In contrast, although the SMX molecule was presented as a completely deprotonated form when pH increased to 7.0 and it possessed higher reactivity than protonated forms [70], PMS showed the poorest stability when pH was 9.0 and where half of HSO_5^- was inclined to decompose to SO_5^{2-} [70], which might be a reason that the catalytic degradation rate decreased from $2.84 \pm 0.22735\text{ min}^{-1}$ to $1.93 \pm 0.07983\text{ min}^{-1}$ as the initial pH increased from 3.0 to 9.0.

In practical engineering applications, the co-existing substances in wastewater might possess undesirable impact on the elimination of target pollutants. Therefore, the influence of inorganic anions including SO_4^{2-} , $H_2PO_4^-$, Cl^- , HCO_3^- , NO_3^- as well as HA on the SMX removal was particularly evaluated. As shown in Fig. 6(b), SO_4^{2-} , $H_2PO_4^-$, Cl^- , HCO_3^- and NO_3^- did not show remarkable effects on the elimination of SMX,

revealing that an outstanding anti-interference capacity of the $Fe_3C/Fe@N-C-9 + PMS$ reaction system. In general, Cl^- was inclined to react with SO_4^{2-} and $\cdot OH$ to produce $Cl\cdot$, $Cl_2\cdot^-$ and $ClOH\cdot^-$ radicals with weaker oxidation abilities, giving rise to an inhibitory effect on the decomposition of organic contaminants [5]. Nevertheless, this inhibition cannot be found in the $Fe_3C/Fe@N-C-9 + PMS$ system, revealing that SO_4^{2-} and $\cdot OH$ were not responsible for SMX removal in this study. As to HCO_3^- , it was a representative dual-function inorganic anion [47]. On the one hand, HCO_3^- acted as an efficient quencher for SO_4^{2-} and $\cdot OH$, but the observed negligible inhibition effect further indicated that the contribution of ROSs-dominated catalytic oxidation process in this system was limited. On the other hand, the solution pH value will inevitably increase by addition of HCO_3^- , which was disadvantageous for SMX removal as mentioned above, thus the corresponding k_1 value slightly dropped to 1.87 min^{-1} . Moreover, the co-existence of SO_4^{2-} , $H_2PO_4^-$ and NO_3^- had no impact on SMX removal, suggesting that the $Fe_3C/Fe@N-C-9 + PMS$ catalytic oxidation system did not depend on active free radicals. And it had been reported that the inhibitory effect of $H_2PO_4^-$ in nonradical-dominated catalytic process was insignificant [47]. Therefore, combined with the above analysis, the degradation of SMX scarcely disturbed by the co-existence of inorganic anions. In addition, HA was chosen as a NOM to evaluate its influence on $Fe_3C/Fe@N-C-9 + PMS$ system. As depicted in Fig. 6(b), the introduction of 10 mg/L of HA could exert negative effect on SMX removal, but 81.3% of SMX can still be removed with 10 min. Such a disadvantageous performance caused by the presence of HA could be ascribed to the competition effect between HA and SMX on the surface of $Fe_3C/Fe@N-C-9$ via strong π - π stacking, resulting in restricting the interaction between PMS and heterogeneous catalytic sites [71]. Besides, HA can

also suppress the SMX oxidation via consumption of $^1\text{O}_2$ [51], which implied that the mechanisms of non-radical pathways in accounting for the SMX degradation should be given serious attention.

Furthermore, the constructed $\text{Fe}_3\text{C}/\text{Fe@N-C-9}$ + PMS reaction system was also effectual for elimination of different types of organic pollutants via PMS activation, such as an organic dye (RhB), a fluoroquinolone antibiotic (CIP), tetracycline (TCH) and a typical endocrine disrupting chemical (BPA), as depicted in Fig. 6(c). Moreover, for the purpose of investigating the mineralization capacities of the $\text{Fe}_3\text{C}/\text{Fe@N-C-9}$ + PMS system toward the above-mentioned organic compounds, the TOC concentrations of aqueous solution before and after catalytic reaction were also analyzed. As illustrated in Fig. S9, the considerable mineralization capacities (above 70.2%) revealed its applicability towards considerable decontamination and detoxification abilities. Meanwhile, it was worth pointing out that the $\text{Fe}_3\text{C}/\text{Fe@N-C-x}$ catalysts can effectively overcome the hurdles of ferric cations leaching. As shown in Fig. 6(d), ICP-OES results indicated that the ferric leaching concentrations for $\text{Fe}_3\text{C}/\text{Fe@N-C-7}$, $\text{Fe}_3\text{C}/\text{Fe@N-C-8}$ and $\text{Fe}_3\text{C}/\text{Fe@N-C-9}$ after catalytic processes were 1.64 ± 0.01226 , 1.43 ± 0.02001 and 0.18 ± 0.02106 mg/L, respectively, which was in compliance with the environmental standard (2 mg/L) established by the European Union [72]. The trace ferric leaching of $\text{Fe}_3\text{C}/\text{Fe@N-C-9}$ definitely benefited from the extraordinary structure of Fe^0 or Fe_3C nanoparticles encapsulated in NCNTs, which should be good for electron transfer and ultimately improving the catalytic activity [73]. Thus, the $\text{Fe}_3\text{C}/\text{Fe@N-C-9}$ + PMS system was a high-potential system for decontamination of wastewater under complicated conditions.

3.3. Mechanisms of enhanced catalytic performances

3.3.1. Singlet oxygen evolution

To further clarify the catalytic degradation mechanisms, the free radical scavenging activity test was conducted to validate the creation mechanisms of reactive species by the $\text{Fe}_3\text{C}/\text{Fe@N-C-9}$ + PMS system. Particularly, MeOH was frequently used as a probe for both $\text{SO}_4^{\cdot-}$ ($k = 9.7 \times 10^8 \text{ M}^{-1}\text{s}^{-1}$) and $\cdot\text{OH}$ ($k = 2.5 \times 10^7 \text{ M}^{-1}\text{s}^{-1}$), respectively [74]. And TBA was deemed as a reasonable capture agent for $\cdot\text{OH}$ ($k = 3.8\text{--}7.6 \times 10^8 \text{ M}^{-1}\text{s}^{-1}$) and less sensitive for $\text{SO}_4^{\cdot-}$ ($k = 4.0\text{--}9.1 \times 10^5 \text{ M}^{-1}\text{s}^{-1}$) [75]. As shown in Fig. 7(a), the introduction of 1 mM of MeOH or TBA (MeOH:PMS = 10, TBA:PMS = 10) exhibited a negligible impact on SMX degradation. In comparison with the controlled experiment, the corresponding k_1 values merely declined from $2.84 \pm 0.22735 \text{ min}^{-1}$ to 2.83 ± 0.02066 or $2.83 \pm 0.04225 \text{ min}^{-1}$ after adding MeOH or TBA, respectively, revealing that only tiny amounts of $\text{SO}_4^{\cdot-}$ and $\cdot\text{OH}$ radicals were generated during the catalytic process. This speculation was further affirmed by continually increasing MeOH and TBA to 10 mM (MeOH:PMS = 100, TBA:PMS = 100) and 100 mM (MeOH:PMS = 1000, TBA:PMS = 1000). It can be clearly observed that the inhibition effects on SMX degradation rate still kept slight, demonstrating that the $\cdot\text{OH}$ and $\text{SO}_4^{\cdot-}$ were not indispensable for the reduction of SMX molecules. To deeply identify the roles of $\cdot\text{OH}$ and $\text{SO}_4^{\cdot-}$, ESR spectra were recorded and DMPO was selected as a spin trapping agent. As shown in Fig. 7(b), the DMPO- $\cdot\text{OH}$ adducts with the characteristic intensities of 1:2:2:1 along with DMPO- $\text{SO}_4^{\cdot-}$ adducts were observed in the $\text{Fe}_3\text{C}/\text{Fe@N-C-9}$ + PMS system, but the corresponding peak intensities was insignificant. This result can also unambiguously confirm that $\text{SO}_4^{\cdot-}$ and $\cdot\text{OH}$ were not the predominant ROSSs in the

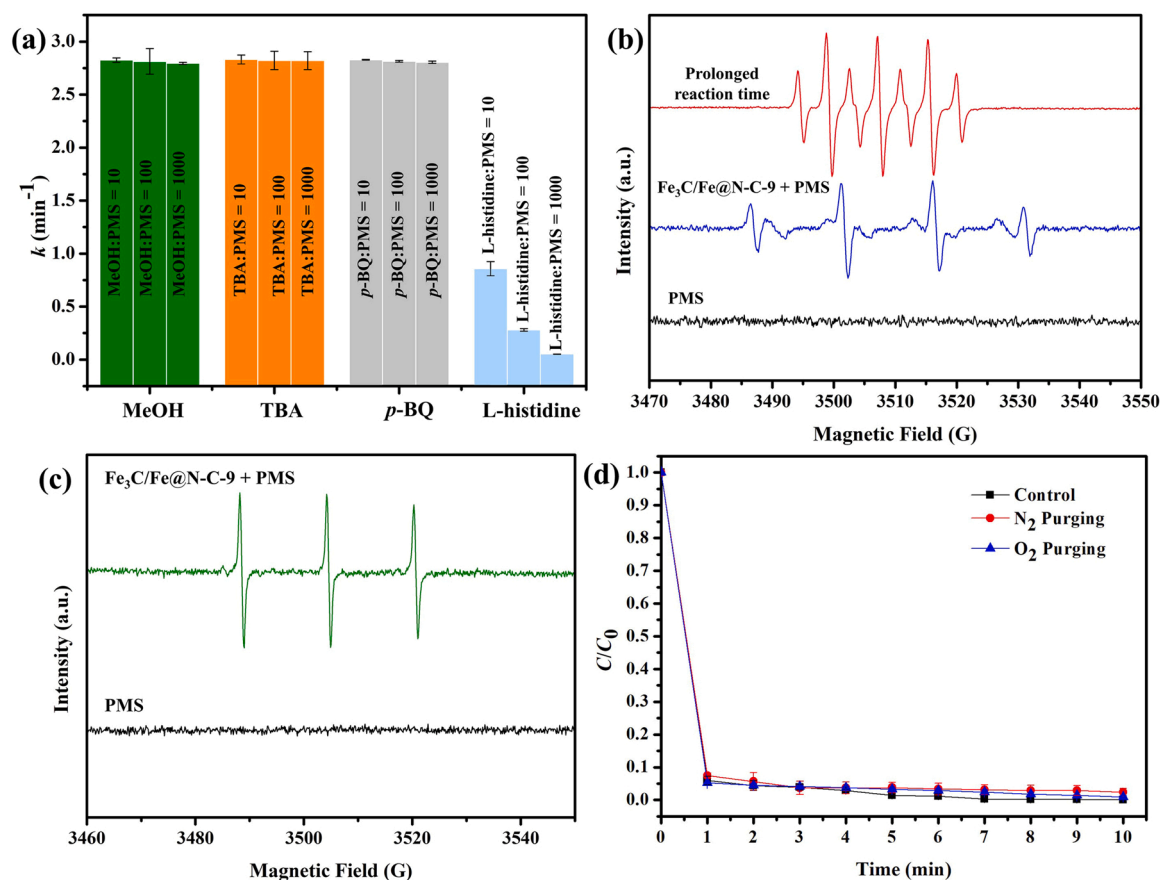


Fig. 7. (a) SMX degradation with various scavengers, such as MeOH, TBA, p -BQ and L-histidine, (b) ESR spectra of obtained at different reaction time using DMPO as spin-trapping agents, (c) ESR spectra of $^1\text{O}_2$ signals in $\text{Fe}_3\text{C}/\text{Fe@N-C-9}$ + PMS system and (d) SMX degradation curves over $\text{Fe}_3\text{C}/\text{Fe@N-C-9}$ + PMS system under different atmospheres. $[\text{PMS}]_0 = 0.1 \text{ mM}$, $[\text{SMX}]_0 = 20 \text{ mg/L}$, $\text{Fe}_3\text{C}/\text{Fe@N-C-9} = 0.3 \text{ g/L}$, $[\text{DMPO}]_0 = [\text{TEMP}]_0 = 50 \text{ mM}$.

$\text{Fe}_3\text{C}/\text{Fe@N-C-9}$ + PMS system. Considering that a small quantity of ferrous leaching from $\text{Fe}_3\text{C}/\text{Fe@N-C-9}$ (0.18 ± 0.02106 mg/L), thereby the corresponding ROSs might be originated from the PMS homogeneous activation. More importantly, the characteristic peaks attributed to 5,5-dimethyl-L-pyrrolidone-2-oxyl (DMPOX) with the intensity ratio of 1:2:1:2:1 can be captured with the prolonging of reaction time. This experimental phenomenon indicated that DMPO should be immediately oxidized rather than being attacked by free radicals during the catalytic processes [52]. Previous reports suggested the oxidized derivative DMPOX was mainly formed by the reaction between DMPO and $^1\text{O}_2$, carbon surface-bound oxidative complexes or Fe-N_x sites [57]. Therefore, it could be considered that the SMX molecules were catalytically degraded through non-radical processes.

Non-radical mediated PMS activation has been reported in different catalysis reaction systems, which can be classified as $^1\text{O}_2$ [51], high-valent iron-oxo complex [42,52] or electron-transfer [10,12]. Therefore, ESR test with TEMP as a capture agent was used to acquire more proofs for the produced reactive species via non-radical process. As shown in Fig. 7(c), 1:1:1 triplet characteristic spectrum assigned to $\text{TEMP-}^1\text{O}_2$ adduct was not captured in PMS alone reaction system, while the signal enhancement of $\text{TEMP-}^1\text{O}_2$ adduct can be detected after the addition of $\text{Fe}_3\text{C}/\text{Fe@N-C-9}$, revealing that the generation of abundant $^1\text{O}_2$. Nevertheless, previous work pointed out the TEMPO adduct might be generated through electron transfer [52]. Thus we selected L-histidine as $^1\text{O}_2$ scavenger, although L-histidine was easy to react with PMS unavoidably ($k = 10.9 \text{ M}^{-1}\text{s}^{-1}$), it tended to preferentially react with $^1\text{O}_2$ at a much higher reaction rate ($k = 3.2 \times 10^7 \text{ M}^{-1}\text{s}^{-1}$) [17]. As shown in Fig. 6(a), the addition of a small quantity of L-histidine (1 mM, L-histidine:PMS = 10) led to a remarkable reduction in catalytic efficiency, only 63.2% of SMX can be degraded by $\text{Fe}_3\text{C}/\text{Fe@N-C-9}$ + PMS system and the corresponding k_1 decreased to $0.86 \pm 0.06755 \text{ min}^{-1}$. While L-histidine was further increased to 10 or 100 mM (L-histidine:PMS = 100 or 1000), the SMX removal efficiency decreased to 26.0% or 4.6% and the k_1 values further decreased to 0.28 ± 0.01203 or $0.05 \pm 0.00106 \text{ min}^{-1}$, respectively. Therefore, it can be concluded that $^1\text{O}_2$ was generated and it played a decisive role in removing SMX by the $\text{Fe}_3\text{C}/\text{Fe@N-C-9}$ + PMS system. Additionally, although L-histidine displayed a strong affinity with $\cdot\text{OH}$ ($k = 5 \times 10^9 \text{ M}^{-1}\text{s}^{-1}$) [57], the inappreciable inhibition effects of MeOH and TBA demonstrated that the quenching experiments by introducing L-histidine were still credible.

Typically, $^1\text{O}_2$ evolution pathways including the self-decomposition of PMS [46,70], the reaction between PMS and some reactive groups (O-C=O , C=O , Fe-N_x , graphitic N, etc.) [17], as well as the photo-excitation of oxygen molecules via an energy-transfer pathway [46,70]. And $^1\text{O}_2$ is mainly derived from three species, such as $\cdot\text{O}_2^-$, dissolved oxygen and $\text{SO}_5^{\cdot-}$ [51]. To elucidate the evolution pathway of $^1\text{O}_2$, *p*-BQ, a selective scavenger of $\cdot\text{O}_2^-$ was tried to exert disadvantageous effects on decomposition of SMX [51]. As depicted in Fig. 6(a), the catalytic rates of SMX were not inhibited by 1 mM, 10 mM and 100 mM of *p*-BQ, which excluded the presence of $\cdot\text{O}_2^-$ during $^1\text{O}_2$ generation. Moreover, as dissolved oxygen might contribute to the $^1\text{O}_2$ generation, thus the elimination of SMX molecules was investigated in different atmospheres. As depicted in Fig. 7(d), the N_2 and O_2 atmospheres did not affect the SMX removal efficiencies, indicating that $^1\text{O}_2$ was not generated from dissolved oxygen. Therefore, we proposed that the $^1\text{O}_2$ was mainly generated via the direct decomposition of PMS over $\text{Fe}_3\text{C}/\text{Fe@N-C-9}$ and derived from $\text{SO}_5^{\cdot-}$ radicals.

According to the linear correlation analysis (Fig. 5(c)), we speculated that $^1\text{O}_2$ might be produced from the following pathways (as illustrated in Fig. 8). Firstly, the abundant C- π active sites on the surface of $\text{Fe}_3\text{C}/\text{Fe@N-C-9}$ can successfully activate PMS to generate $\text{SO}_5^{\cdot-}$ radicals, as expressed by Eqs. (2) and (3) [76,77]. Because the rapid reaction rate ($k = 2.0 \times 10^8 \text{ M}^{-1}\text{s}^{-1}$) and low activation energy ($E = 7.4 \pm 2.4 \text{ kcal/mol}$), rapid self-reaction of $\text{SO}_5^{\cdot-}$ will contribute to produce $^1\text{O}_2$ (Eqs. (4) and (5)) [51]. It should be noted that in such reaction circumstance, the produced $\text{SO}_4^{\cdot-}$ radicals were inclined to be scavenged

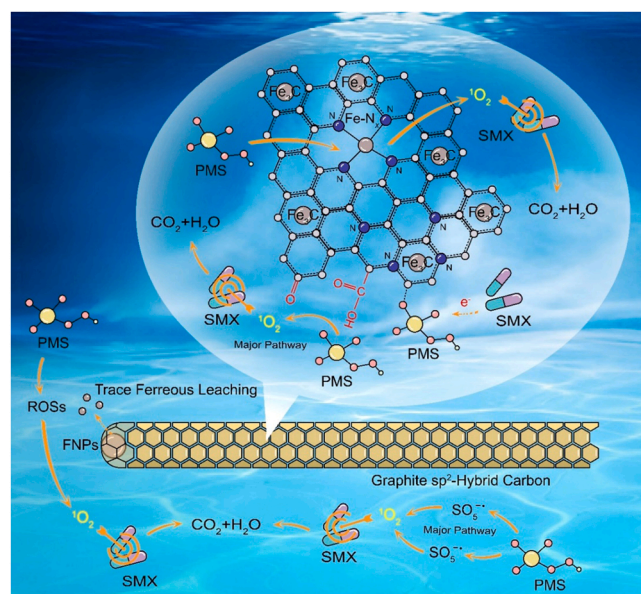
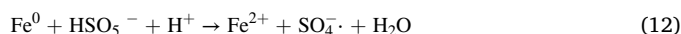
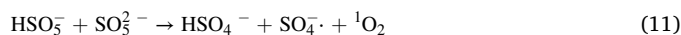
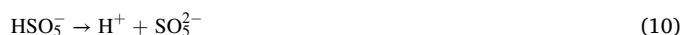
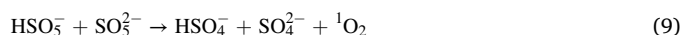
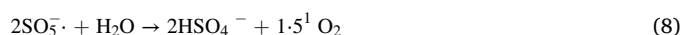
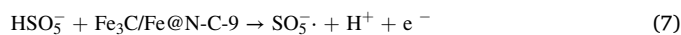
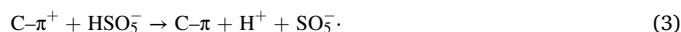
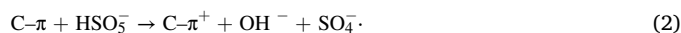


Fig. 8. Proposed catalytic mechanisms in $\text{Fe}_3\text{C}/\text{Fe@N-C-9}$ + PMS reaction system.

by PMS to generate $\text{SO}_5^{\cdot-}$ with a low oxidative potential (1.1 V) and high reaction rate ($k = 1.0 \times 10^5 \text{ M}^{-1}\text{s}^{-1}$) through Eq. (6) [78], instead of directly acting on the oxidation of SMX. Because the kinetic constants in SMX degradation process significantly increased from $0.89 \pm 0.00560 \text{ min}^{-1}$ at 0.025 mM PMS to $2.53 \pm 0.08216 \text{ min}^{-1}$ at 0.075 mM PMS (Fig. S10). However, only a slight increase of kinetic constant was observed when the PMS concentration further increased to 0.1 mM. This experimental phenomenon revealed that the PMS concentration (0.1 mM) used in the catalytic reactions was sufficient.

Secondly, the oxygen groups (O-C=O and C=O) of $\text{Fe}_3\text{C}/\text{Fe@N-C-9}$ can serve as the catalysis sites for direct decomposing PMS to generation of $^1\text{O}_2$ [17,79,80]. The O atoms in O-C=O together with N atoms connected to Fe-N_4 sites might act as electron acceptors to deplete the adsorbed PMS for the generation of $\text{SO}_5^{\cdot-}$. It will further react with H_2O to generate $^1\text{O}_2$, as described by Eqs. (7) and (8) [81]. Meanwhile, C=O was prone to activate PMS to generate $^1\text{O}_2$ through Eq. (9) [77,82], which could also contribute to SMX degradation via the non-radical pathway. Thirdly, the self-decomposition of PMS can also dedicate to the formation of $^1\text{O}_2$ (Eqs. (10) and (11)). At last, the mere existence of Fe leaching in reaction solution and trace amount of Fe^0 species can induce $\text{SO}_4^{\cdot-}$ or $\cdot\text{OH}$, and subsequently transformed into $^1\text{O}_2$ (Eqs. (12)–(16)) [83].





3.3.2. Electron-transfer mechanism

As mentioned in Section 3.2.1, the catalytic activation of PMS over $\text{Fe}_3\text{C}/\text{Fe@N-C-9}$ for SMX removal was a two-stage-reaction. Therefore, electron transfer might contribute to the second stage of SMX removal, since $\text{Fe}_3\text{C}/\text{Fe@N-C-9}$ was constituted of sp^2 -conjugated carbons [12], active N species (graphitic N and Fe-N_4) [52] and Fe_3C with strong abilities for electron transfer [53]. In this study, the electron-transfer mechanism was confirmed by electrochemical measurements and *in-situ* Raman spectral analysis. As shown in Fig. 9(a), a remarkable increase of the current density can be observed when $\text{Fe}_3\text{C}/\text{Fe@N-C-9}$, SMX and PMS were simultaneously added, suggesting a current flow was formed in metastable reactive complex ($\text{Fe}_3\text{C}/\text{Fe@N-C-9-PMS}^*$) [12, 16]. Moreover, a smaller semicircle diameter in EIS can be achieved by the $\text{Fe}_3\text{C}/\text{Fe@N-C-9} + \text{PMS} + \text{SMX}$ system (as illustrated in Fig. 9(b)), indicating that faster interfacial charge transfer between the $\text{Fe}_3\text{C}/\text{Fe@N-C-9-PMS}^*$ and SMX was possible [52]. Besides, the *i-t* curve was used to record the current changes after introducing PMS and SMX at a specific open-circuit voltage (Fig. 9(c)). It can be seen that no obvious fluctuation of current after the introduction of PMS, but the current decreased sharply after the addition of SMX, implying that the co-adsorption behavior of PMS and SMX on the surface of $\text{Fe}_3\text{C}/\text{Fe@N-C-9}$ was inclined to induce the electron-transfer pathway, which

was in line with the ESR analysis about the clear signal of DMPOX [12]. In addition, the generation of $\text{Fe}_3\text{C}/\text{Fe@N-C-9-PMS}^*$ metastable complex was directly confirmed by *in-situ* Raman spectroscopy. As shown in Fig. 9(d), the peaks at 889 and 1060 cm^{-1} originated from HSO_5^- , and a strong peak at 983 cm^{-1} should be attributed to SO_4^{2-} [84]. Interestingly, when the $\text{Fe}_3\text{C}/\text{Fe@N-C-9}$ was added into the PMS solution, a new peak at 839 cm^{-1} was detected, which was due to the bending vibration of the metal-peroxo bonds, affirming the presence of the $\text{Fe}_3\text{C}/\text{Fe@N-C-9-PMS}^*$ complex [12]. The above electrochemical and *in-situ* Raman results demonstrated that $\text{Fe}_3\text{C}/\text{Fe@N-C-9}$ can also activate PMS through an electron-mediated non-radical pathway. The formed $\text{Fe}_3\text{C}/\text{Fe@N-C-9-PMS}^*$ complex can elevate the redox potential of the $\text{Fe}_3\text{C}/\text{Fe@N-C-9}$ ($E_{\text{Fe}_3\text{C}/\text{Fe@N-C-9}}$), when $E_{\text{Fe}_3\text{C}/\text{Fe@N-C-9}}$ exceeded the oxidation potential of the SMX (E_{SMX}), the $\text{Fe}_3\text{C}/\text{Fe@N-C-9-PMS}^*$ complex will extract electrons from the SMX and SMX was easy to decompose via the electron transfer process. Moreover, as shown in Fig. S6, $\text{Fe}_3\text{C}/\text{Fe@N-C-9}$ possessed larger k_2 values ($0.50 \pm 0.01757 \text{ min}^{-1}$) than those of $\text{Fe}_3\text{C}/\text{Fe@N-C-7}$ ($0.01 \pm 0.00078 \text{ min}^{-1}$) and $\text{Fe}_3\text{C}/\text{Fe@N-C-8}$ ($0.02 \pm 0.00639 \text{ min}^{-1}$). This result can be attributed to the following reasons: (1) higher adsorption capacity was achieved by $\text{Fe}_3\text{C}/\text{Fe@N-C-9}$ (Fig. 4(a)). Thus stronger pre-adsorption effect was beneficial to the subsequent catalytic process; (2) higher O—C=O content (2.12 at%) in $\text{Fe}_3\text{C}/\text{Fe@N-C-9}$ can improve the hydrophilicity and accelerate mass transfer of SMX/PMS on the surface [12]; (3) more defects in $\text{Fe}_3\text{C}/\text{Fe@N-C-7}$ and $\text{Fe}_3\text{C}/\text{Fe@N-C-8}$ (confirmed by Raman analysis) might cause partial carbon transformation from sp^2 to sp^3 , which might deteriorate the electron-transfer process [85]; (4) more importantly, benefited from the CNT morphology of $\text{Fe}_3\text{C}/\text{Fe@N-C-9}$ and its higher complete sp^2 -hybridized structure, the

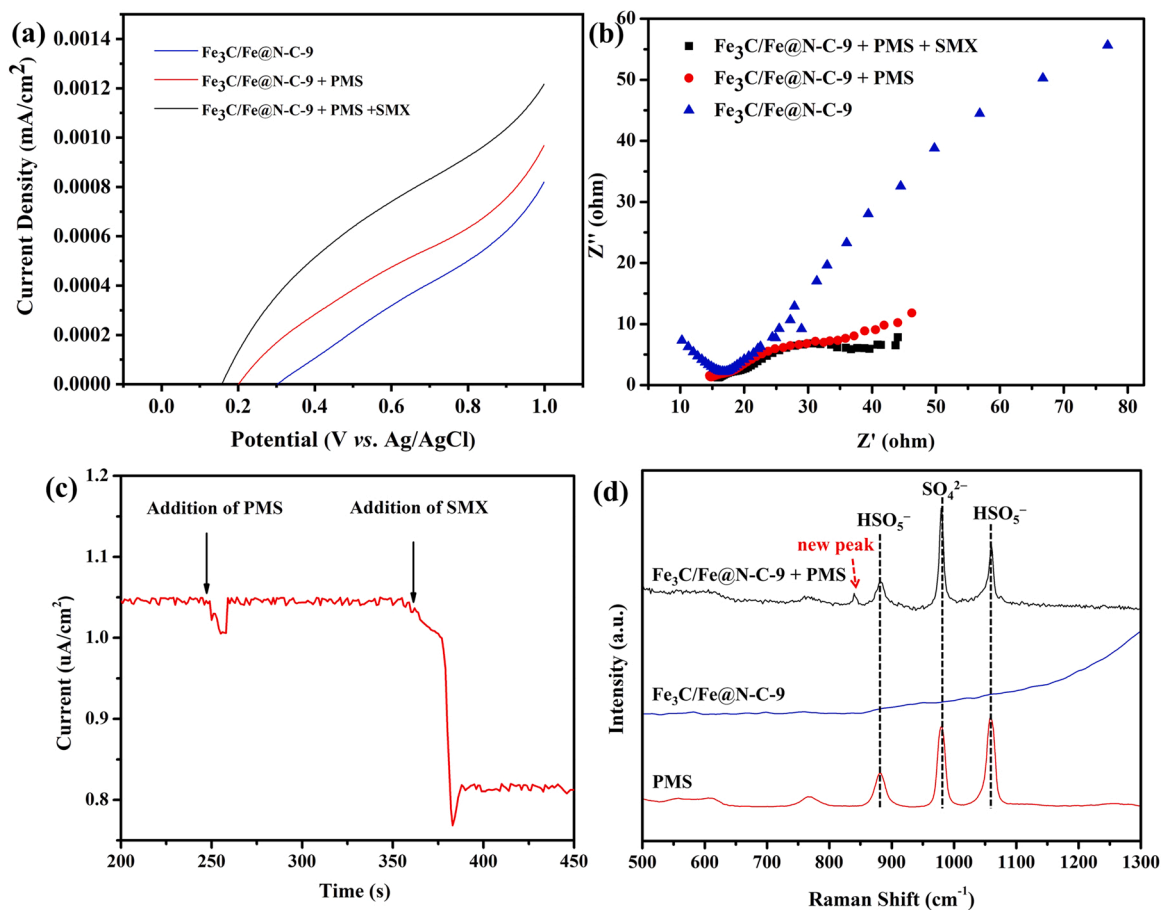


Fig. 9. (a) LSV curves, (b) EIS analysis, (c) current response curves after addition of PMS and SMX at the $\text{Fe}_3\text{C}/\text{Fe@N-C-9}$ electrode in solution, $[\text{PMS}]_0 = 1.5 \text{ mM}$, $[\text{SMX}]_0 = 5.0 \text{ mg/L}$, (d) *in-situ* Raman spectra obtained in different reaction systems.

entrapped FNPs can impressively modulate the electronic states of the interacted carbon regions, giving rise to faster electron transfer efficiency with synergistic promotion of N-doping. The $\text{Fe}_3\text{C}/\text{Fe@N-C-9}$ possessed the highest current density in LSV curves and the smallest semicircle diameter in EIS analysis (Fig. S11), which further confirmed that the $\text{Fe}_3\text{C}/\text{Fe@N-C-9}$ had greater charge transfer ability.

3.3.3. Identification the role of HV-Fe

Previous studies reported that HV-Fe species ($\text{Fe}^{\text{V}}=\text{O}$ and $\text{Fe}^{\text{IV}}=\text{O}$) in Fe-based catalysts can directly degrade organic pollutants [42,86]. To explore possible HV-Fe components, PMSO_2 was used as the HV-Fe probe in different reaction systems [87]. As shown in Fig. 10(a), PMSO_2 production was not enhanced in the $\text{Fe}_3\text{C}/\text{Fe@N-C-9}$ + PMS system in contrast to the PMS alone system, suggesting that the HV-Fe was not formed during the heterogeneous catalytic process. Furthermore, HV-Fe was also detected by the a selective scavenger, DMSO [52]. As illustrated in Fig. 10(b), the SMX removal rates were not distinctly reduced along with DMSO increased from 1 to 100 mM (the ratio of DMSO:PMS increased from 10 to 1000), suggesting the absence of HV-Fe in $\text{Fe}_3\text{C}/\text{Fe@N-C-9}$ sample. Moreover, effect of oxalate on SMX removal was explored since the active iron sites were inclined to coordinate with carboxyl groups of oxalate, leading to the target pollutants removal will be terminated in HV-Fe dominated catalytic process [87]. As displayed in Fig. 10(b), the SMX degradation rates were slightly suppressed after adding oxalate in $\text{Fe}_3\text{C}/\text{Fe@N-C-9}$ + PMS system, even though the ratio of oxalate:PMS increased to 40, confirming that HV-Fe was not involved in the catalytic process. To sum up, $^1\text{O}_2$ evolution and electron-transfer were the dominant non-radical pathways occurred in $\text{Fe}_3\text{C}/\text{Fe@N-C-9}$ + PMS + SMX reaction system.

3.4. Practical application evaluation

From the aspect of actual practices, the reusability of a catalyst is crucial for remediation of water environments. Bearing this in mind, continuous running experiments were conducted to assess the stability of $\text{Fe}_3\text{C}/\text{Fe@N-C-9}$ catalyst. As shown in Fig. 11(a), the $\text{Fe}_3\text{C}/\text{Fe@N-C-9}$ could be repeatedly used as an efficient catalyst for PMS activation and the removal efficiency of SMX still maintained at 81.2% after 5 runs. The decreased degradation efficiency might be ascribed to co-adsorption of SMX or catalytic intermediates on the surface of $\text{Fe}_3\text{C}/\text{Fe@N-C-9}$ and a small amount of lost catalytic sites. Furthermore, the magnetic properties of the $\text{Fe}_3\text{C}/\text{Fe@N-C-x}$ materials were characterized by VSM. The M-H curves in Fig. 11(b) demonstrated nonlinear and reversible behaviors with robust saturation magnetizations of 51.04, 59.74 and 121.78 emu/g for $\text{Fe}_3\text{C}/\text{Fe@N-C-7}$, $\text{Fe}_3\text{C}/\text{Fe@N-C-8}$ and $\text{Fe}_3\text{C}/\text{Fe@N-C-9}$, respectively. Owing to the encapsulated Fe_3C and Fe^0 nanoparticles beneath

the graphitic carbon shells, which allowed the $\text{Fe}_3\text{C}/\text{Fe@N-C-9}$ to be easily recovered by an external magnetic field without needless separation process (the insert of Fig. 11(b)). Moreover, the PXRD patterns (Fig. 11(c)) and morphology (Fig. S12) of the $\text{Fe}_3\text{C}/\text{Fe@N-C-9}$ before and after catalysis had good coincidence, indicating that the $\text{Fe}_3\text{C}/\text{Fe@N-C-9}$ did not undergo phase transformation and the skeleton structure was maintained well. Additionally, the XPS spectra of the used $\text{Fe}_3\text{C}/\text{Fe@N-C-9}$ were tested, as illustrated in Fig. S13. The relative contents of the different species occupying in the total elements for used $\text{Fe}_3\text{C}/\text{Fe@N-C-9}$ were shown in Table S2. For C 1 s, the amount of C- π dropped to 36.4%, indicating that the C- π played an important role in the catalytic reaction. And after the catalytic reaction, the ratios of O-C=O and C=O groups were also observed to decrease, suggesting that these oxygen-containing groups interacted with PMS and mediated non-radical processes. With respect to N 1 s and Fe 2p, the relative contents of graphitic N, pyridinic N and Fe-N_x declined, meanwhile the ratio of $\text{Fe}^{3+}/\text{Fe}^{2+}$ decreased from 1.43 to 0.86. The obtained results revealed that the above species also participated in PMS activation process.

More importantly, to further evaluate the application potential of $\text{Fe}_3\text{C}/\text{Fe@N-C-9}$ + PMS system in a complicated water environment, the removal efficiency of actual pharmaceutical wastewater was analyzed. Its background concentrations of inorganic ions were shown in Table S3. Meanwhile, based on the ultra-performance liquid chromatography tandem triple quadrupole mass spectrometry analysis technology of 80 antibiotics built by our laboratory, the antibiotics in the actual pharmaceutical wastewater were screened and analyzed combined with the information of the standard sample. If the parent ions and fragment ions of the compound appeared simultaneously and the HPLC retention time was consistent with that of the standard, the organic compound was considered to be detected. As shown in Fig. S14, the detected antibiotics were sulfadoxine, doxycycline and 2-aminoflubenazole, and their basic properties were illustrated in Table S4. Fig. 11(d) depicted the performance of $\text{Fe}_3\text{C}/\text{Fe@N-C-9}$ + PMS system on removal of COD from the actual pharmaceutical wastewater. The removal percentage reached 43.4% with the $\text{Fe}_3\text{C}/\text{Fe@N-C-9}$ dosage of 0.3 g/L and PMS initial concentration of 5 mM. And the color of the sample changed from yellow to colorless after catalytic reaction (as shown in insert of Fig. 10(d)). It was worthy to noting that the removal efficiency of COD in the actual pharmaceutical wastewater was much lower than that in the simulated sample by spiking modeling organic pollutants into ultrapure water. It could be ascribed to that the co-existing dissolved organic matters (DOM) interfered with degradation of antibiotics via PMS consumption or reducing antibiotics' susceptibilities to reactive species like $^1\text{O}_2$ [71].

To verify the above speculations, EEM spectroscopy was applied to monitor DOM in actual wastewater samples. Because the high COD

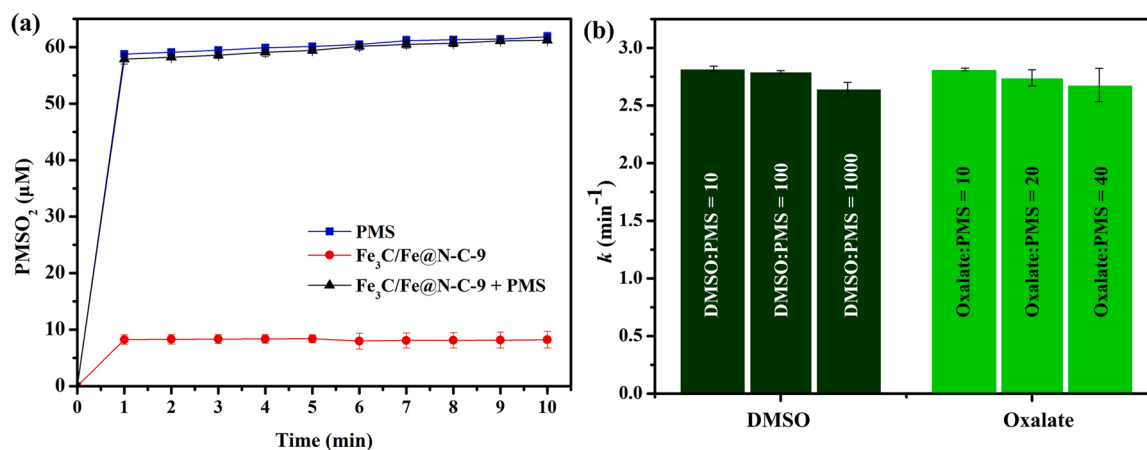


Fig. 10. (a) PMSO_2 production in different reaction systems. $[\text{PMSO}_2]_0 = 1000 \mu\text{M}$, $[\text{PMS}]_0 = 0.1 \text{ mM}$, $\text{Fe}_3\text{C}/\text{Fe@N-C-9} = 0.3 \text{ g/L}$, (b) the corresponding kinetic reaction constants obtained by the presence of different scavengers, such as DMSO and oxalate.

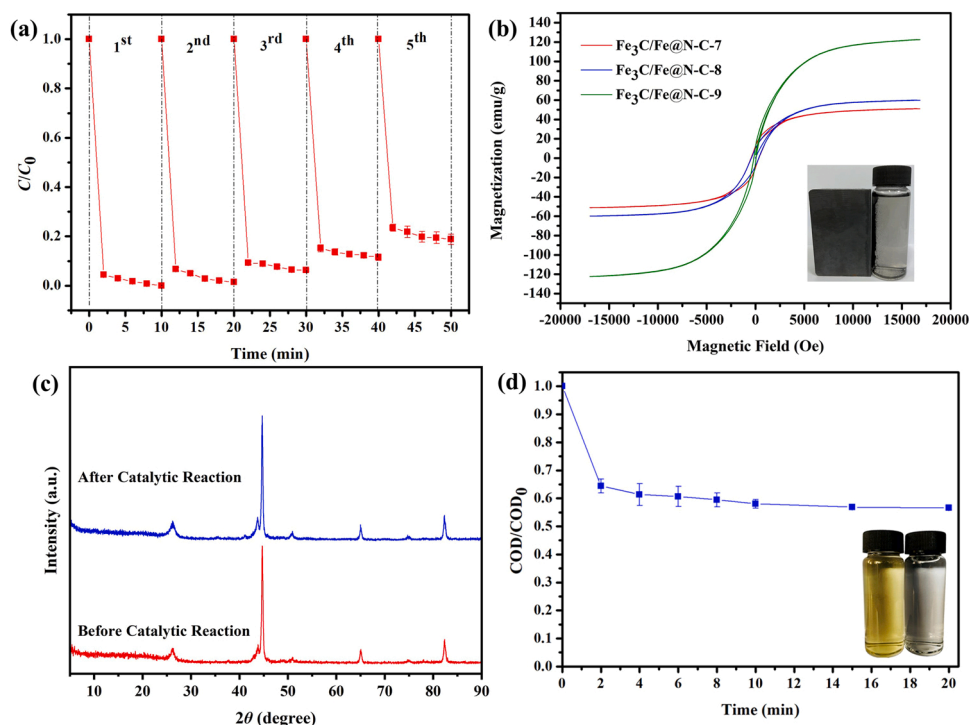


Fig. 11. (a) Reusability of the $\text{Fe}_3\text{C}/\text{Fe@N-C-9}$ catalyst for the degradation of SMX, (b) magnetic properties of the as-prepared $\text{Fe}_3\text{C}/\text{Fe@N-C-x}$ catalysts, (c) PXRD patterns of $\text{Fe}_3\text{C}/\text{Fe@N-C-9}$ before and after catalytic process and (d) the COD removal efficiencies in actual pharmaceutical wastewater by $\text{Fe}_3\text{C}/\text{Fe@N-C-9} + \text{PMS}$ system.

concentration of original sample (in excess of 10000 mg/L), it was gradually diluted by 2000 times to avoid inner-filter effect for subsequent analysis. The EEM spectrum of original pharmaceutical wastewater sample was shown in Fig. 12(a), the peak at E_x/E_m of 260–275/400–450 nm was related to soluble-microbial-byproduct (SMP)-like components [61], while the peak at E_x/E_m of 310–325/400–430 nm was associated with fulvic-like fluorophores [61]. The fluorescence intensities of the above characteristic peaks were 1470 and 350 QSU, respectively. After treated with $\text{Fe}_3\text{C}/\text{Fe@N-C-9} + \text{PMS}$ system for 10 min, the corresponding intensities of the two characteristic peaks rapidly dropped to 654 and 190 QSU (Fig. 12(b)), respectively. As a whole, being compared with other (PS-AOPs), such as ionizing radiation- [22,88] and UV-assisted technologies [89,90], the constructed

$\text{Fe}_3\text{C}/\text{Fe@N-C-9} + \text{PMS}$ system can purify the pharmaceutical wastewater with relatively acceptable efficiency and lower energy cost.

4. Conclusion

In summary, a sequence of $\text{Fe}_3\text{C}/\text{Fe@N-C-x}$ catalysts were fabricated by using MIL-88B(Fe) as a self-sacrificing template and melamine as a N-doping precursor in a ball-milling pretreatment and one-pot calcination procedure. The characterization results showed that all the $\text{Fe}_3\text{C}/\text{Fe@N-C-x}$ catalysts underwent distinct changes in physical and chemical properties after the pyrolysis process. In particular, benefitted from the synergistic effect of the sp^2 -hybridized carbon network, oxygen-containing groups, N-doping species, Fe_3C and Fe^0 nanoparticles

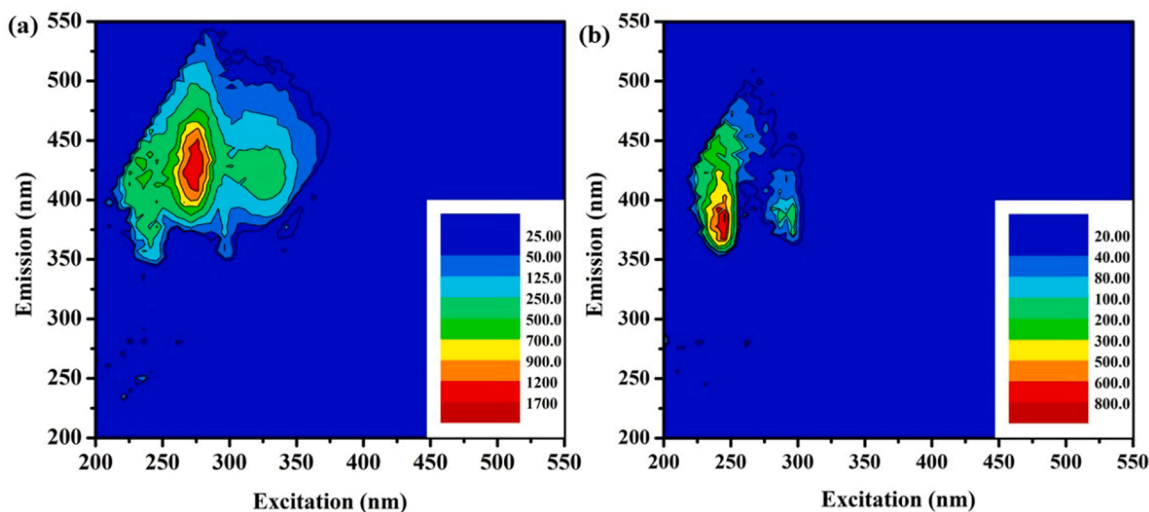


Fig. 12. (a)-(b) EEM spectra of pharmaceutical wastewater samples before and after treatment by $\text{Fe}_3\text{C}/\text{Fe@N-C-9} + \text{PMS}$ system. $[\text{PMS}]_0 = 0.1 \text{ mM}$, $\text{Fe}_3\text{C}/\text{Fe@N-C-9} = 0.3 \text{ g/L}$.

encapsulated in NCNTs, the Fe₃C/Fe@N-C-9 possessed an excellent ability for ultrafast removal of emerging contaminants via PMS activation. Meanwhile, the Fe₃C/Fe@N-C-9 attained little Fe leakage in reaction solution. The catalytic mechanisms were investigated by means of quenching tests, ESR signals, electrochemical analysis and *in-situ* Raman spectroscopy. Both ¹O₂ evolution and electron transfer were validated to the SMX removal by Fe₃C/Fe@N-C-9 + PMS system. The effects of environmental factors (initial pH, inorganic anions and NOM) on the catalytic degradation process were analyzed. The results revealed the constructed Fe₃C/Fe@N-C-9 + PMS system can achieve considerable degradation efficiency for modeling organic compounds in complicated water matrices. Moreover, the Fe₃C/Fe@N-C-9 + PMS system could also decontaminate real pharmaceutical wastewater with an appreciable degradation efficiency. This research offered a new perspective about the catalytic degradation of organic pollutants triggered by MOFs-derived materials, which verified the feasibility of MOFs-PMS-based reaction systems for future treatment of organic wastewater.

CRedit authorship contribution statement

Chen Zhao: Data curation, Investigation, Visualization, Writing – original draft preparation. **Linghui Meng:** Instrumental, Investigation. **Hongyu Chu:** Instrumental, Investigation. **Jian-Feng Wang:** Resources, Instrumental. **Tianyu Wang:** Instrumental. **Yuhui Ma:** Resources, Instrumental. **Chong-Chen Wang:** Conceptualization, Funding acquisition, Supervision, Project administration, Writing – review & editing.

Declaration of Competing Interest

The authors declare that they have no known competing financial interests or personal relationships that could have appeared to influence the work reported in this paper.

Data availability

Data will be made available on request.

Acknowledgments

This work was supported by National Natural Science Foundation of China (22176012, 51878023), Beijing Natural Science Foundation (8202016), Great Wall Scholars Training Program Project of Beijing Municipality Universities (CIT&TCD20180323), Beijing Talent Project (2020A27), Science and Technology General Project of Beijing Municipal Education Commission (KM202110016010), the Fundamental Research Funds for Beijing University of Civil Engineering and Architecture (X20147/X20141/X20135/X20146).

Appendix A. Supporting information

Supplementary data associated with this article can be found in the online version at [doi:10.1016/j.apcatb.2022.122034](https://doi.org/10.1016/j.apcatb.2022.122034).

References

- [1] L. García, J.C. Leyva-Díaz, E. Díaz, S. Ordóñez, A review of the adsorption-biological hybrid processes for the abatement of emerging pollutants: Removal efficiencies, physicochemical analysis, and economic evaluation, *Sci. Total Environ.* 780 (2021), 146554.
- [2] C.-Y. Wang, L. Ma, C.-C. Wang, P. Wang, L. Gutierrez, W. Zheng, Light-response adsorption and desorption behaviors of metal-organic frameworks, *Environ. Funct. Mater.* 1 (2022) 49–66.
- [3] D.B. Miklos, C. Remy, M. Jekel, K.G. Linden, J.E. Drewes, U. Hübner, Evaluation of advanced oxidation processes for water and wastewater treatment – A critical review, *Water Res.* 139 (2018) 118–131.
- [4] R. Su, L. Huang, N. Li, L. Li, B. Jin, W. Zhou, B. Gao, Q. Yue, Q. Li, Chlorine dioxide radicals triggered by chlorite under visible-light irradiation for enhanced degradation and detoxification of norfloxacin antibiotic: Radical mechanism and toxicity evaluation, *Chem. Eng. J.* 414 (2021), 128768.
- [5] C. Zhao, J. Wang, X. Chen, Z. Wang, H. Ji, L. Chen, W. Liu, C.-C. Wang, Bifunctional Bi₁₂O₁₇C₁₂/MIL-100(Fe) composites toward photocatalytic Cr(VI) sequestration and activation of persulfate for bisphenol A degradation, *Sci. Total Environ.* 752 (2021), 141901.
- [6] L. Liu, X. Xu, Y. Li, R. Su, Q. Li, W. Zhou, B. Gao, Q. Yue, One-step synthesis of “nuclear-shell” structure iron-carbon nanocomposite as a persulfate activator for bisphenol A degradation, *Chem. Eng. J.* 382 (2020), 122780.
- [7] H. Lan, J. Zhou, Z. Hou, X. An, H. Liu, J. Qu, Defect modulation of MOF-derived ZnFe₂O₄/CNTs microcages for persulfate activation: Enhanced nonradical catalytic oxidation, *Chem. Eng. J.* 431 (2022), 133369.
- [8] X. Duan, H. Sun, Z. Shao, S. Wang, Nonradical reactions in environmental remediation processes: Uncertainty and challenges, *Appl. Catal. B Environ.* 224 (2018) 973–982.
- [9] M. Kohantorabi, G. Moussavi, S. Giannakis, A review of the innovations in metal- and carbon-based catalysts explored for heterogeneous peroxymonosulfate (PMS) activation, with focus on radical vs. non-radical degradation pathways of organic contaminants, *Chem. Eng. J.* 411 (2021), 127957.
- [10] W. Ren, L. Xiong, X. Yuan, Z. Yu, H. Zhang, X. Duan, S. Wang, Activation of peroxydisulfate on carbon nanotubes: electron-transfer mechanism, *Environ. Sci. Technol.* 53 (2019) 14595–14603.
- [11] J. Lee, U. von Gunten, J.-H. Kim, Persulfate-based advanced oxidation: critical assessment of opportunities and roadblocks, *Environ. Sci. Technol.* 54 (2020) 3064–3081.
- [12] W. Ren, C. Cheng, P. Shao, X. Luo, H. Zhang, S. Wang, X. Duan, Origins of electron-transfer regime in persulfate-based nonradical oxidation processes, *Environ. Sci. Technol.* 56 (2022) 78–97.
- [13] H. Sun, S. Liu, G. Zhou, H.M. Ang, M.O. Tadé, S. Wang, Reduced graphene oxide for catalytic oxidation of aqueous organic pollutants, *ACS Appl. Mater. Interfaces* 4 (2012) 5466–5471.
- [14] H. Lee, H.-i Kim, S. Weon, W. Choi, Y.S. Hwang, J. Seo, C. Lee, J.-H. Kim, Activation of persulfates by graphitized nanodiamonds for removal of organic compounds, *Environ. Sci. Technol.* 50 (2016) 10134–10142.
- [15] Y. Hu, D. Chen, R. Zhang, Y. Ding, Z. Ren, M. Fu, X. Cao, G. Zeng, Singlet oxygen-dominated activation of peroxymonosulfate by passion fruit shell derived biochar for catalytic degradation of tetracycline through a non-radical oxidation pathway, *J. Hazard. Mater.* 419 (2021), 126495.
- [16] S. Zhu, X. Huang, F. Ma, L. Wang, X. Duan, S. Wang, Catalytic Removal of Aqueous Contaminants on N-Doped Graphitic Biochars: Inherent Roles of Adsorption and Nonradical Mechanisms, *Environ. Sci. Technol.* 52 (2018) 8649–8658.
- [17] N. Li, R. Li, X. Duan, B. Yan, W. Liu, Z. Cheng, G. Chen, L. Hou, S. Wang, Correlation of active sites to generated reactive species and degradation routes of organics in peroxymonosulfate activation by co-loaded carbon, *Environ. Sci. Technol.* 55 (2021) 16163–16174.
- [18] J. Deng, P. Ren, D. Deng, L. Yu, F. Yang, X. Bao, Highly active and durable non-precious-metal catalysts encapsulated in carbon nanotubes for hydrogen evolution reaction, *Energy Environ. Sci.* 7 (2014) 1919–1923.
- [19] J. Deng, D. Deng, X. Bao, Robust Catalysis on 2D Materials Encapsulating Metals: Concept, Application, and Perspective, *Adv. Mater.* 29 (2017), 1606967.
- [20] X. Duan, S. Indrawirawan, H. Sun, S. Wang, Effects of nitrogen-, boron-, and phosphorus-doping or codoping on metal-free graphene catalysis, *Catal. Today* 249 (2015) 184–191.
- [21] W. Tian, H. Zhang, H. Sun, A. Suvorova, M. Saunders, M. Tade, S. Wang, Heteroatom (N or S)-Doping Induced Layered and Honeycomb Microstructures of Porous Carbons for CO₂ Capture and Energy Applications, *Adv. Funct. Mater.* 26 (2016) 8651–8661.
- [22] S. Zhang, Y. Zhuo, C.I. Ezugwu, C.-c. Wang, C. Li, S. Liu, Synergetic Molecular Oxygen Activation and Catalytic Oxidation of Formaldehyde over Defective MIL-88B(Fe) Nanorods at Room Temperature, *Environ. Sci. Technol.* 55 (2021) 8341–8350.
- [23] W. Xia, A. Mahmood, R. Zou, Q. Xu, Metal-organic frameworks and their derived nanostructures for electrochemical energy storage and conversion, *Energy Environ. Sci.* 8 (2015) 1837–1866.
- [24] P. Horcajada, F. Salles, S. Wuttke, T. Devic, D. Heurtaux, G. Maurin, A. Vimont, M. Daturi, O. David, E. Magnier, N. Stock, Y. Filinchuk, D. Popov, C. Riekell, G. Férey, C. Serre, How Linker's Modification Controls Swelling Properties of Highly Flexible Iron(III) Dicarboxylates MIL-88, *J. Am. Chem. Soc.* 133 (2011) 17839–17847.
- [25] Z. Wu, Y. Liang, X. Yuan, D. Zou, J. Fang, L. Jiang, J. Zhang, H. Yang, Z. Xiao, MXene Ti₃C₂ derived Z-scheme photocatalyst of graphene layers anchored TiO₂/g-C₃N₄ for visible light photocatalytic degradation of refractory organic pollutants, *Chem. Eng. J.* 394 (2020), 124921.
- [26] C. Zhao, Z. Wang, C. Wang, X. Li, C.-C. Wang, Photocatalytic degradation of DOM in urban stormwater runoff with TiO₂ nanoparticles under UV light irradiation: EEM-PARAFAC analysis and influence of co-existing inorganic ions, *Environ. Pollut.* 243 (2018) 177–188.
- [27] M. Li, Z. Li, X. Yu, Y. Wu, C. Mo, M. Luo, L. Li, S. Zhou, Q. Liu, N. Wang, K. Lun Yeung, S. Chen, FeN₄-doped carbon nanotubes derived from metal organic frameworks for effective degradation of organic dyes by peroxymonosulfate: Impacts of FeN₄ spin states, *Chem. Eng. J.* 431 (2022), 133339.
- [28] T. Zeng, M. Yu, H. Zhang, Z. He, J. Chen, S. Song, Fe/Fe₃C@N-doped porous carbon hybrids derived from nano-scale MOFs: robust and enhanced heterogeneous catalyst for peroxymonosulfate activation, *Catal. Sci. Technol.* 7 (2017) 396–404.
- [29] M. Zhao, H. Song, Synthesis of carbon-encapsulated iron carbide/iron nanoparticles from phenolic-formaldehyde resin and ferric nitrate, *Mater. Chem. Phys.* 124 (2010) 861–864.

- [30] K.K. Pandey, A study of chemical structure of soft and hardwood and wood polymers by FTIR spectroscopy, *J. Appl. Polym. Sci.* 71 (1999) 1969–1975.
- [31] P. Huang, P. Zhang, C. Wang, J. Tang, H. Sun, Enhancement of persulfate activation by Fe-biochar composites: Synergism of Fe and N-doped biochar, *Appl. Catal. B Environ.* 303 (2022), 120926.
- [32] P. Gayathri, A.S. Kumar, An iron impurity in multiwalled carbon nanotube complexes with chitosan that biomimics the heme-peroxidase function, *Chem. Eur. J.* 19 (2013) 17103–17112.
- [33] Z.-H. Sheng, L. Shao, J.-J. Chen, W.-J. Bao, F.-B. Wang, X.-H. Xia, Catalyst-free synthesis of nitrogen-doped graphene via thermal annealing graphite oxide with melamine and its excellent electrocatalysis, *ACS Nano* 5 (2011) 4350–4358.
- [34] D. Nuvoli, L. Valentini, V. Alzari, S. Scognamiglio, S.B. Bon, M. Piccinini, J. Illescas, A. Mariani, High concentration few-layer graphene sheets obtained by liquid phase exfoliation of graphite in ionic liquid, *J. Mater. Chem.* 21 (2011) 3428–3431.
- [35] S. Dissegna, K. Epp, W.R. Heinz, G. Kieslich, R.A. Fischer, Defective metal-organic frameworks, *Adv. Mater.* 30 (2018), 1704501.
- [36] X. Li, J. Zhang, L. Shen, Y. Ma, W. Lei, Q. Cui, G. Zou, Preparation and characterization of graphitic carbon nitride through pyrolysis of melamine, *Appl. Phys. A* 94 (2009) 387–392.
- [37] B. Zhang, R. Chen, Z. Yang, Y. Chen, L. Zhou, Y. Yuan, Melamine-assisted synthesis of paper mill sludge-based carbon nanotube/nanoporous carbon nanocomposite for enhanced electrocatalytic oxygen reduction activity, *Int. J. Hydrog. Energ.* 44 (2019) 31094–31103.
- [38] Y. Yao, B. Zhang, J. Shi, Q. Yang, Preparation of nitrogen-doped carbon nanotubes with different morphologies from melamine-formaldehyde resin, *ACS Appl. Mater. Inter.* 7 (2015) 7413–7420.
- [39] J. Kang, L. Zhou, X. Duan, H. Sun, Z. Ao, S. Wang, Degradation of cosmetic microplastics via functionalized carbon nanospings, *Matter* 1 (2019) 745–758.
- [40] X. Li, F. Liao, L. Ye, L. Yeh, Controlled pyrolysis of MIL-88A to prepare iron/carbon composites for synergistic persulfate oxidation of phenol: Catalytic performance and mechanism, *J. Hazard. Mater.* 398 (2020), 122938.
- [41] Q. Lai, L. Zheng, Y. Liang, J. He, J. Zhao, J. Chen, Metal–Organic-Framework-Derived Fe-N/C Electrocatalyst with Five-Coordinated Fe-N_x Sites for Advanced Oxygen Reduction in Acid Media, *ACS Catal.* 7 (2017) 1655–1663.
- [42] Y. Li, T. Yang, S. Qiu, W. Lin, J. Yan, S. Fan, Q. Zhou, Uniform N-coordinated single-atomic iron sites dispersed in porous carbon framework to activate PMS for efficient BPA degradation via high-valent iron-oxo species, *Chem. Eng. J.* 389 (2020), 124382.
- [43] D. Ding, S. Yang, X. Qian, L. Chen, T. Cai, Nitrogen-doping positively whilst sulfur-doping negatively affect the catalytic activity of biochar for the degradation of organic contaminant, *Appl. Catal. B Environ.* 263 (2020), 118348.
- [44] G. Yang, J. Dong, B. Xing, S. Mo, X. Song, X. Liu, J. Yuan, Ni, Fe, and N-tridoped activated carbon as a highly active heterogeneous persulfate catalyst toward the degradation of organic pollutant in water, *Sep. Purif. Technol.* 252 (2020), 117440.
- [45] X. Li, Y. Jia, M. Zhou, X. Su, J. Sun, High-efficiency degradation of organic pollutants with Fe, N co-doped biochar catalysts via persulfate activation, *J. Hazard. Mater.* 397 (2020), 122764.
- [46] X. Duan, Z. Ao, H. Sun, S. Indrawirawan, Y. Wang, J. Kang, F. Liang, Z.H. Zhu, S. Wang, Nitrogen-Doped Graphene for Generation and Evolution of Reactive Radicals by Metal-Free Catalysis, *ACS Appl. Mater. Inter.* 7 (2015) 4169–4178.
- [47] X. Duan, Z. Ao, L. Zhou, H. Sun, G. Wang, S. Wang, Occurrence of radical and nonradical pathways from carbocatalysts for aqueous and nonaqueous catalytic oxidation, *Appl. Catal. B Environ.* 188 (2016) 98–105.
- [48] M. Pu, J. Wan, F. Zhang, M.L. Brusseau, D. Ye, J. Niu, Insight into degradation mechanism of sulfamethoxazole by metal-organic framework derived novel magnetic Fe@C composite activated persulfate, *J. Hazard. Mater.* 414 (2021), 125598.
- [49] D. Archundia, C. Duwig, L. Spadini, M.C. Morel, B. Prado, M.P. Perez, V. Orsag, J. M.F. Martins, Assessment of the Sulfamethoxazole mobility in natural soils and of the risk of contamination of water resources at the catchment scale, *Environ. Int.* 130 (2019), 104905.
- [50] Y. Shang, C. Chen, P. Zhang, Q. Yue, Y. Li, B. Gao, X. Xu, Removal of sulfamethoxazole from water via activation of persulfate by Fe₃C@NCNTs including mechanism of radical and nonradical process, *Chem. Eng. J.* 375 (2019), 122004.
- [51] L.-S. Zhang, X.-H. Jiang, Z.-A. Zhong, L. Tian, Q. Sun, Y.-T. Cui, X. Lu, J.-P. Zou, S.-L. Luo, Carbon Nitride Supported High-Loading Fe Single-Atom Catalyst for Activation of Peroxymonosulfate to Generate ¹O₂ with 100% Selectivity, *Angew. Chem. Int. Ed.* 60 (2021) 21751–21755.
- [52] T. Yang, S. Fan, Y. Li, Q. Zhou, Fe-N/C single-atom catalysts with high density of Fe-N_x sites toward peroxymonosulfate activation for high-efficient oxidation of bisphenol A: Electron-transfer mechanism, *Chem. Eng. J.* 419 (2021), 129590.
- [53] T. Xiao, Y. Wang, J. Wan, Y. Ma, Z. Yan, S. Huang, C. Zeng, Fe-N-C catalyst with Fe-N_x sites anchored nano carbon cubes derived from Fe-Zn-MOFs activate peroxymonosulfate for high-effective degradation of ciprofloxacin: Thermal activation and catalytic mechanism, *J. Hazard. Mater.* 424 (2022), 127380.
- [54] X. Zou, X. Huang, A. Goswami, R. Silva, B.R. Sathe, E. Mikmeková, T.J.A.C. Asefa, Cobalt-embedded nitrogen-rich carbon nanotubes efficiently catalyze hydrogen evolution reaction at all pH values, *Angew. Chem. Int. Ed.* 126 (2014) 4461–4465.
- [55] X. Duan, H. Sun, S. Wang, Metal-Free Carbocatalysis in Advanced Oxidation Reactions, *Acc. Chem. Res.* 51 (2018) 678–687.
- [56] J. Ye, J. Dai, C. Li, Y. Yan, Lawn-like Co₃O₄@N-doped carbon-based catalytic self-cleaning membrane with peroxymonosulfate activation: A highly efficient singlet oxygen dominated process for sulfamethoxazole degradation, *Chem. Eng. J.* 421 (2021), 127805.
- [57] Y. Li, J. Li, Y. Pan, Z. Xiong, G. Yao, R. Xie, B. Lai, Peroxymonosulfate activation on FeCo₂S₄ modified g-C₃N₄ (FeCo₂S₄-CN): Mechanism of singlet oxygen evolution for nonradical efficient degradation of sulfamethoxazole, *Chem. Eng. J.* 384 (2020), 123361.
- [58] J. Yan, J. Li, J. Peng, H. Zhang, Y. Zhang, B. Lai, Efficient degradation of sulfamethoxazole by the CuO@Al₂O₃ (EPC) coupled PMS system: Optimization, degradation pathways and toxicity evaluation, *Chem. Eng. J.* 359 (2019) 1097–1110.
- [59] M. Xu, J. Li, Y. Yan, X. Zhao, J. Yan, Y. Zhang, B. Lai, X. Chen, L. Song, Catalytic degradation of sulfamethoxazole through peroxymonosulfate activated with expanded graphite loaded CoFe₂O₄ particles, *Chem. Eng. J.* 369 (2019) 403–413.
- [60] S. Wang, Y. Liu, J. Wang, Iron and sulfur co-doped graphite carbon nitride (FeOy/S-g-C₃N₄) for activating peroxymonosulfate to enhance sulfamethoxazole degradation, *Chem. Eng. J.* 382 (2020), 122836.
- [61] C.-M. Hung, C.-W. Chen, C.-P. Huang, S. Shiung Lam, C.-D. Dong, Peroxymonosulfate activation by a metal-free biochar for sulfonamide antibiotic removal in water and associated bacterial community composition, *Bioresour. Technol.* 343 (2022), 126082.
- [62] Y. Wang, Y. Song, N. Li, W. Liu, B. Yan, Y. Yu, L. Liang, G. Chen, La Hou, S. Wang, Tunable active sites on biogas digestate derived biochar for sulfanilamide degradation by peroxymonosulfate activation, *J. Hazard. Mater.* 421 (2022), 126794.
- [63] W. Zhu, S. Ndayiragije, X. Zuo, X. Zhang, G. Wang, X. Wang, ZIF-8-derived single-atom Cu and N co-coordinated porous carbon as bifunctional material for SMX removal, *J. Environ. Chem. Eng.* 10 (2022), 107758.
- [64] C. Li, J. Wu, W. Peng, Z. Fang, J. Liu, Peroxymonosulfate activation for efficient sulfamethoxazole degradation by Fe₃O₄/β-FeOOH nanocomposites: Coexistence of radical and non-radical reactions, *Chem. Eng. J.* 356 (2019) 904–914.
- [65] H. Zeng, L. Deng, K. Yang, B. Huang, H. Zhang, Z. Shi, W. Zhang, Degradation of sulfamethoxazole using peroxymonosulfate activated by self-sacrificed synthesized CoAl-LDH@CoFe-PBA nanosheet: Reactive oxygen species generation routes at acidic and alkaline pH, *Sep. Purif. Technol.* 268 (2021), 118654.
- [66] S. Wang, Y. Liu, J. Wang, Peroxymonosulfate Activation by Fe-Co-O-Codoped Graphite Carbon Nitride for Degradation of Sulfamethoxazole, *Environ. Sci. Technol.* 54 (2020) 10361–10369.
- [67] X. Ao, Z. Li, H. Zhang, A comprehensive insight into a rapid degradation of sulfamethoxazole by peroxymonosulfate enhanced UV-A LED/g-C₃N₄ photocatalysis, *J. Clean. Prod.* 356 (2022), 131822.
- [68] S. Cai, X. Zuo, H. Zhao, S. Yang, R. Chen, L. Chen, R. Zhang, D. Ding, T. Cai, Evaluation of N-doped carbon for the peroxymonosulfate activation and removal of organic contaminants from livestock wastewater and groundwater, *J. Mater. Chem. A* 10 (2022) 9171–9183.
- [69] S. Mei, J. Gu, T. Ma, X. Li, Y. Hu, W. Li, J. Zhang, Y. Han, N-doped activated carbon from used dyeing wastewater adsorbent as a metal-free catalyst for acetylene hydrochlorination, *Chem. Eng. J.* 371 (2019) 118–129.
- [70] J. Wang, S. Wang, Activation of persulfate (PS) and peroxymonosulfate (PMS) and application for the degradation of emerging contaminants, *Chem. Eng. J.* 334 (2018) 1502–1517.
- [71] X. Yang, F.L. Rosario-Ortiz, Y. Lei, Y. Pan, X. Lei, P. Westerhoff, Multiple Roles of Dissolved Organic Matter in Advanced Oxidation Processes, *Environ. Sci. Technol.* 56 (2022) 11111–11131.
- [72] J.-W. Wang, F.-G. Qiu, P. Wang, C. Ge, C.-C. Wang, Boosted bisphenol A and Cr(VI) cleanup over Z-scheme WO₃/MIL-100(Fe) composites under visible light, *J. Clean. Prod.* 279 (2021), 123408.
- [73] W.-J. Jiang, L. Gu, L. Li, Y. Zhang, X. Zhang, L.-J. Zhang, J.-Q. Wang, J.-S. Hu, Z. Wei, L.-J. Wan, Understanding the High Activity of Fe-N-C Electrocatalysts in Oxygen Reduction: Fe/Fe₃C Nanoparticles Boost the Activity of Fe-N_x, *J. Am. Chem. Soc.* 138 (2016) 3570–3578.
- [74] Y. Zhou, J. Jiang, Y. Gao, J. Ma, S.-Y. Pang, J. Li, X.-T. Lu, L.-P. Yuan, Activation of peroxymonosulfate by benzoquinone: a novel nonradical oxidation process, *Environ. Sci. Technol.* 49 (2015) 12941–12950.
- [75] Y. Ding, L. Zhu, N. Wang, H. Tang, Sulfate radicals induced degradation of tetrabromobisphenol A with nanoscale magnetic CoFe₂O₄ as a heterogeneous catalyst of peroxymonosulfate, *Appl. Catal. B Environ.* 129 (2013) 153–162.
- [76] E. Saputra, S. Muhammad, H. Sun, S. Wang, Activated carbons as green and effective catalysts for generation of reactive radicals in degradation of aqueous phenol, *RSC Adv.* 3 (2013) 21905–21910.
- [77] Y. Zhang, H. Pan, M. Murugananthan, P. Sun, D.D. Dionysiou, K. Zhang, A. Khan, Y. Zhang, Glucose and melamine derived nitrogen-doped carbonaceous catalyst for nonradical peroxymonosulfate activation, *Carbon* 156 (2020) 399–409.
- [78] G. Wang, S. Chen, X. Quan, H. Yu, Y. Zhang, Enhanced activation of peroxymonosulfate by nitrogen doped porous carbon for effective removal of organic pollutants, *Carbon* 115 (2017) 730–739.
- [79] H. Meng, C. Nie, W. Li, X. Duan, B. Lai, Z. Ao, S. Wang, T. An, Insight into the effect of lignocellulosic biomass source on the performance of biochar as persulfate activator for aqueous organic pollutants remediation: Epicarp and mesocarp of citrus peels as examples, *J. Hazard. Mater.* 399 (2020), 123043.
- [80] W. Liu, C. Nie, W. Li, Z. Ao, S. Wang, T. An, Oily sludge derived carbons as peroxymonosulfate activators for removing aqueous organic pollutants: Performances and the key role of carbonyl groups in electron-transfer mechanism, *J. Hazard. Mater.* 414 (2021), 125552.
- [81] Y. Gao, Y. Zhu, L. Lyu, Q. Zeng, X. Xing, C. Hu, Electronic Structure Modulation of Graphitic Carbon Nitride by Oxygen Doping for Enhanced Catalytic Degradation of Organic Pollutants through Peroxymonosulfate Activation, *Environ. Sci. Technol.* 52 (2018) 14371–14380.

- [82] P. Shao, J. Tian, F. Yang, X. Duan, S. Gao, W. Shi, X. Luo, F. Cui, S. Luo, S. Wang, Identification and Regulation of Active Sites on Nanodiamonds: Establishing a Highly Efficient Catalytic System for Oxidation of Organic Contaminants, *Adv. Funct. Mater.* 28 (2018), 1705295.
- [83] C. Dong, Y. Bao, T. Sheng, Q. Yi, Q. Zhu, B. Shen, M. Xing, I.M.C. Lo, J. Zhang, Singlet oxygen triggered by robust bimetallic MoFe/TiO₂ nanospheres of highly efficacy in solar-light-driven peroxymonosulfate activation for organic pollutants removal, *Appl. Catal. B Environ.* 286 (2021), 119930.
- [84] S. Zhu, P. Xiao, X. Wang, Y. Liu, X. Yi, H. Zhou, Efficient peroxymonosulfate (PMS) activation by visible-light-driven formation of polymorphic amorphous manganese oxides, *J. Hazard. Mater.* 427 (2022), 127938.
- [85] Q. Yang, Y. Chen, X. Duan, S. Zhou, Y. Niu, H. Sun, L. Zhi, S. Wang, Unzipping carbon nanotubes to nanoribbons for revealing the mechanism of nonradical oxidation by carbocatalysis, *Appl. Catal. B Environ.* 276 (2020), 119146.
- [86] J. Li, H. Lan, W. Zhang, X. An, H. Liu, J. Qu, Characterization on the formation mechanism of Fe₀/Fe₃C/C nanostructure and its effect on PMS activation performance towards BPA degradation, *Chem. Eng. J.* 435 (2022), 134709.
- [87] P. Duan, J. Pan, W. Du, Q. Yue, B. Gao, X. Xu, Activation of peroxymonosulfate via mediated electron transfer mechanism on single-atom Fe catalyst for effective organic pollutants removal, *Appl. Catal. B Environ.* 299 (2021), 120714.
- [88] L. Chu, J. Wang, C. Chen, S. He, L. Wojnárovits, E. Takács, Advanced treatment of antibiotic wastewater by ionizing radiation combined with peroxymonosulfate/H₂O₂, *Oxid., J. Clean. Prod.* 321 (2021), 128921.
- [89] A. Eslami, M. Hashemi, F. Ghanbari, Degradation of 4-chlorophenol using catalyzed peroxymonosulfate with nano-MnO₂/UV irradiation: Toxicity assessment and evaluation for industrial wastewater treatment, *J. Clean. Prod.* 195 (2018) 1389–1397.
- [90] S. Giannakis, K.-Y.A. Lin, F. Ghanbari, A review of the recent advances on the treatment of industrial wastewaters by Sulfate Radical-based Advanced Oxidation Processes (SR-AOPs), *Chem. Eng. J.* 406 (2021), 127083.